JAMES | Journal of Advances in Modeling Earth Systems

RESEARCH ARTICLE
10.1029/2024MS004804

Confronting Large-Eddy Simulations With Stereo Camera Data by Means of Reconstructed Hemispheric Cloud Size Distributions

Yannick Burchart[1], **Bernhard Pospichal**[1], **and Roel A. J. Neggers**[1]

[1]Institute for Geophysics and Meteorology, University of Cologne, Cologne, Germany

Key Points:

- A hemispheric camera simulator is used to compare large-eddy simulations with real-world observations of shallow cumulus clouds over land
- 3D cloud reconstruction is applied to both real and rendered images, yielding intrinsically comparable cloud size distributions
- These hemispheric size distributions agree well between model and observations, and follow distinct power law functional forms

Correspondence to:
Y. Burchart,
yburchar@uni-koeln.de

Citation:
Burchart, Y., Pospichal, B., & Neggers, R. A. J. (2025). Confronting large-eddy simulations with stereo camera data by means of reconstructed hemispheric cloud size distributions. *Journal of Advances in Modeling Earth Systems*, *17*, e2024MS004804. https://doi.org/10.1029/2024MS004804

Received 28 OCT 2024
Accepted 8 JUN 2025

Author Contributions:
Conceptualization: Yannick Burchart, Roel A. J. Neggers
Data curation: Yannick Burchart
Formal analysis: Yannick Burchart, Bernhard Pospichal
Funding acquisition: Roel A. J. Neggers
Investigation: Yannick Burchart
Methodology: Yannick Burchart, Bernhard Pospichal, Roel A. J. Neggers
Project administration: Roel A. J. Neggers
Resources: Yannick Burchart, Bernhard Pospichal, Roel A. J. Neggers
Software: Yannick Burchart, Roel A. J. Neggers
Supervision: Roel A. J. Neggers
Validation: Yannick Burchart, Bernhard Pospichal, Roel A. J. Neggers

Abstract High-resolution hemispheric camera images at a meteorological site in western Germany are used to analyze the multi-dimensional spatial characteristics of continental cumulus cloud fields, and to evaluate Large-Eddy Simulations on this aspect. Traditional non-hemispheric cloud-detecting instruments provide additional reference data. The main model-observation comparison focuses on cloud size distributions (CSDs), employing two methods: (a) directly using three-dimensional model fields, *direct CSDs*, and (b) using rendered hemispheric images of the model fields as produced by a camera simulator based on path-tracing. In the latter method, both the real and rendered images are used to three-dimensionally reconstruct the cloud fields, yielding *hemispheric CSDs*. Advantages of hemispheric comparisons over more classic approaches include (a) fair comparisons between model and data, and (b) full use of the enhanced resolutions and hemispheric spatial coverage of the camera imagery. Basic evaluation of the simulations demonstrates good agreement on thermodynamic structure and its diurnal cycle. Cloud heights and cloud cover are intercompared between the model, camera data and other instrumentation, providing insight into their structural differences. A consistent alignment is found between the hemispheric CSDs from both the model and the cameras. Power law fits reveal structurally lower exponents in hemispheric CSDs compared to non-hemispheric CSDs, which particularly caution against directly comparing hemispheric CSDs to non-hemispheric distributions. This result is robust for sample size and fitting method. These findings inform future use of hemispheric camera systems for studying cumulus cloud field morphology and model evaluation.

Plain Language Summary Cumulus clouds are difficult to model accurately in weather and climate simulations due to their complex and ever-changing structures. Traditional meteorological tools often can't capture these details. To overcome this, we used high-resolution cameras that provide a detailed view of the clouds. In this study, we compared cloud simulations from Large-Eddy Simulations (LES) with real cloud observations from cameras and other instruments in western Germany. We used two methods: the first directly compared the simulation data, and the second involved rendering images from the simulation using a path-tracing algorithm to match the camera's perspective. This helped us to better compare the two data sets. Our results showed that the cloud reconstructions from the simulations closely matched the actual camera images and other ground-based measurements. We also found that the cloud sizes were more accurately captured using the cloud reconstructions from camera data than with direct comparisons of the simulation data. This study is among the first to use camera data for analyzing cloud sizes and it highlights the ability of camera-based methods to capture smaller cloud structures that are often missed by other methods.

1. Introduction

Cumulus clouds (Cu) exert significant influence on Earth's weather and climate, by impacting radiative transfer and facilitating the vertical transport of heat, moisture, and momentum within the lower atmosphere. This makes an accurate representation of cumulus clouds in general circulation models of crucial importance (Myers et al., 2021; Neggers, Neelin, & Stevens, 2007; Nuijens & Siebesma, 2019; Tiedtke, 1989). A complicating factor in this effort is the complex spatial geometry of cumulus cloud fields, which plays a key role in all of their impacts. e.g., radiative transfer is strongly affected by cumulus cloud overlap (e.g., Corbetta et al., 2015), while vertical transport is effected by lateral entrainment across the heterogeneous cloud boundaries (Dawe & Austin, 2013; Garrett et al., 2018).

The importance of Cu cloud geometry has motivated and prioritized efforts to reliably observe this feature with meteorological instrumentation. Traditionally, one-dimensional, vertically pointing remote sensing instruments

Visualization: Yannick Burchart
Writing – original draft: Yannick Burchart
Writing – review & editing: Yannick Burchart, Bernhard Pospichal, Roel A. J. Neggers

have been used to this purpose, including ceilometers, lidars and radars (Fielding et al., 2020; Schulz et al., 2021; Zhan et al., 2021). However, due to their limited Field-Of View (FOV) these techniques struggle to simultaneously detect the potentially complex spatial geometry of the full cloud field, which might be rapidly evolving. An alternative to surface instrumentation is satellite or high-altitude airplane imagery, which have the benefit of covering much larger areas (DeWitt et al., 2024; Plank, 1969; Wood & Field, 2011). A limitation is that such imagery are mainly vertical projections, and until recently also had too limited spatial resolution to detect geometry down to the smallest scale. The typically low time frequency of high altitude imagery also acts to limit their use for fully understanding Cu cloud evolution (Fielding et al., 2020; Schulz et al., 2021).

An attractive alternative for capturing the high resolution complex geometry of Cu cloud fields is stereo photogrammetry (Beekmans et al., 2016; Crispel & Roberts, 2018; Malkus & Ronne, 1954). This optical technique detects much finer spatial details, and images are also available at high frequencies (typically every few seconds). But arguably the biggest advantage is the opportunity it provides to reconstruct geometry in multiple dimensions, including the temporal one. This is enabled by the use of more than one high-frequency camera, with two-camera systems often referred to as stereo cameras (e.g., Beekmans et al., 2016). Recently, networks of multiple cameras have been developed to even further improve the four-dimensional reconstruction of the spatial and temporal features of the observed cloud fields (Blum et al., 2021; Nouri et al., 2019; Öktem & Romps, 2021; Romps & Öktem, 2018). Such large camera networks have successfully provided new insights into the geometric shape and evolution of cumulus clouds.

Apart from observational efforts, high-resolution Large-Eddy Simulation (LES) has proven to be an alternative numerical tool for investigating Cu cloud field geometry. LES offers unlimited access to full four-dimensional virtual cloud fields (Angevine et al., 2018; Neggers et al., 2011; Shen et al., 2022; Siebesma & Jonker, 2000). Profiting from the ongoing surge in the efficiency and capability of High Performance Computing (HPC), increasingly finer resolutions and larger domains are becoming feasible. This gives access to very fine-scale cloud geometry, at least virtually. Despite these significant advantages, LES still remains only a model, per definition being a simplification of reality with inherent limitations. This necessitates validation of LES results on cloud geometry against observational data, a topic which has been intensely researched in recent decades (Griewank et al., 2020; Heinze et al., 2017; Senf et al., 2018).

So far, however, few attempts have been made to confront LES with stereo camera data. Burchart et al. (2024) introduced a novel tool to this purpose, using hemispheric path tracing acting on LES-generated three-dimensional fields of cloud liquid water content. This tool renders virtual images of model clouds in almost exactly the same way a real hemispheric camera would see them, thus functioning as a so-called "instrument simulator" for hemispheric cameras. Such simulators enable a both fair and robust evaluation of cumulus cloud geometry in LES models against high frequency, high-resolution camera network data.

The primary aim of this study is to conduct a statistical comparison of cumulus cloud geometry between hemispheric camera data and LES cloud fields. More specifically, the method developed by Burchart et al. (2024) is adopted to three-dimensionally reconstruct cloud fields from both rendered images from LES fields and real images from a stereo camera system installed at a meteorological site in Germany. The comparison is extended to include data from various other ground-based cloud-observing instrumentation at the site, to provide reference and gain further understanding of how observations of cloud properties fundamentally differ between these systems. The focus lies on two selected consecutive days in July 2021 on which well defined diurnal cycles of boundary layer shallow Cu were observed at the site. On these days, hourly radiosondes were launched to constrain the LES experiments as much as possible with independent observations.

In this study, cloud field geometry is primarily researched by means of the horizontal cloud size distribution (hCSD), defined as the distribution of the square root of the vertically projected cloud areas. Previous research of the hCSD has predominantly relied on satellite data (e.g., DeWitt et al., 2024; Wielicki & Welch, 1986; Yuan, 2011), high-altitude aircraft data (Plank, 1969; Rodts et al., 2003; Wood & Field, 2011) or high-resolution model output (e.g., Heus & Seifert, 2013; Laar et al., 2019; Neggers et al., 2003, 2019; Rieck et al., 2014). Estimating the hCSD from reconstructed cloud fields from camera networks would provide a new independent source of information in addition to the existing data sets, with particular added value provided by the observational coverage of much smaller spatial and temporal scales. It is on this aspect where previous studies of the hCSD have predominantly relied on simulation data. A specific objective of this study is to structurally compare

hCSDs from both the LES and the cameras for the 2 days of interest, including an assessment of how hemispherically derived hCSDs differ from distributions sampled directly from the model output.

The structure of this paper is organized as follows: Section 2 provides a comprehensive description of the meteorological site (Section 2.1), the camera-based cloud field reconstruction (Section 2.2), the observational data (Section 2.3), the LES model setup (Section 2.4), and the algorithm for rendering camera images from LES data (Section 2.5), followed by the retrieval methods for cloud properties (Section 2.6), including cloud cover, cloud base height, and horizontal cloud size distributions. In Section 3, the analysis cases are introduced, accompanied by an initial evaluation of the thermodynamic structure and its diurnal circle. Section 4 presents a comparative analysis of the reconstructions from real and rendered images, alongside data from other ground-based instruments and direct LES outputs. Finally, Section 5 discusses the broader implications of these findings, with conclusions presented in Section 6.

2. Data and Methods

2.1. JOYCE

The Jülich Observatory for Cloud Evolution (JOYCE, Löhnert et al., 2015) is a meteorological mid-latitude continental site located in western Germany. Its relative proximity to the North Sea ensures a persistent supply of low level atmospheric humidity, supporting a frequent occurrence of summertime shallow cumulus convection. These characteristics makes the site well suited for scientific investigation of this cloud regime. The site is operated by the University of Cologne on a continuous, year-round basis, and features a suite of standard and more advanced meteorological instrumentation (described in detail in Section 2.3).

2.2. Camera-Based Cloud Field Reconstruction

The schematic workflow for reconstructing cloud fields from camera images is illustrated in Figure 1. This process is applied to both actual camera observations (see Section 2.3) and images rendered from LES (see Section 2.4 for the model setup and Section 2.5 for the rendering algorithm). Methods common to both data sets are highlighted in green, while data set-specific methods are shown in orange or blue respectively. These data set-specific methods include the Path-Tracing Algorithm for rendering LES images (Section 2.5), the CNN cloud masking algorithm—trained on either actual or rendered images—and the distortion correction algorithms, which account for the optical distortions caused by the cameras' protective glass dome. The latter correction is unnecessary for rendered images, as they are not subject to such distortions.

The common reconstructions steps are rectifying the images by using an epipolar rectification model as described in Beekmans et al. (2016), to a format where cloud displacements are constraint to the x-axis, which is crucial for the inter-camera matching. The Semi-Global Block-Matching algorithm (Hirschmuller, 2005) is then employed to align cloudy pixels between cameras, producing disparity maps that quantify pixel shifts during camera transitions. Triangulation, using both the disparity maps and camera calibration parameters, reconstructs the location of the cloudy pixels in 3D space. The effective Field-Of-View (FOV) used in the reconstruction process is a 6×7 km rectangle. The precision of this reconstruction process relies on the accurate identification of cloudy pixels, as facilitated by the cloud mask. For more details, see Beekmans et al. (2016).

Additionally, minor discrepancies in the matching algorithm occasionally generated small regions with zero pixel displacement within the clouds, leading to fragmented cloud representations in the disparity maps. To address this issue, the reconstruction approach is refined by interpolating the disparity maps within the cloud regions. This refinement involved removing areas of zero pixel displacement and utilizing the Clough-Tocher 2D interpolation method from the SciPy Python library (Virtanen et al., 2020). The cloud masks thereby ensure that interpolation is exclusively performed within cloud areas.

In this study, the reconstruction process is improved by replacing the color-based threshold method used in previous studies (Beekmans et al., 2016; Burchart et al., 2024) with a more advanced CNN for cloud masking. For that, a convolutional neural network (CNN) cloud mask algorithm based on the U-Net architecture is used. This approach is adapted from previous studies, including Fabel et al. (2022), focusing on cloud detection in all-sky imagers, and Drönner et al. (2018), which applied the method to satellite imagery. Unlike Fabel et al. (2022), this study employs a binary classification model that categorizes pixels as either cloudy or non-cloudy.

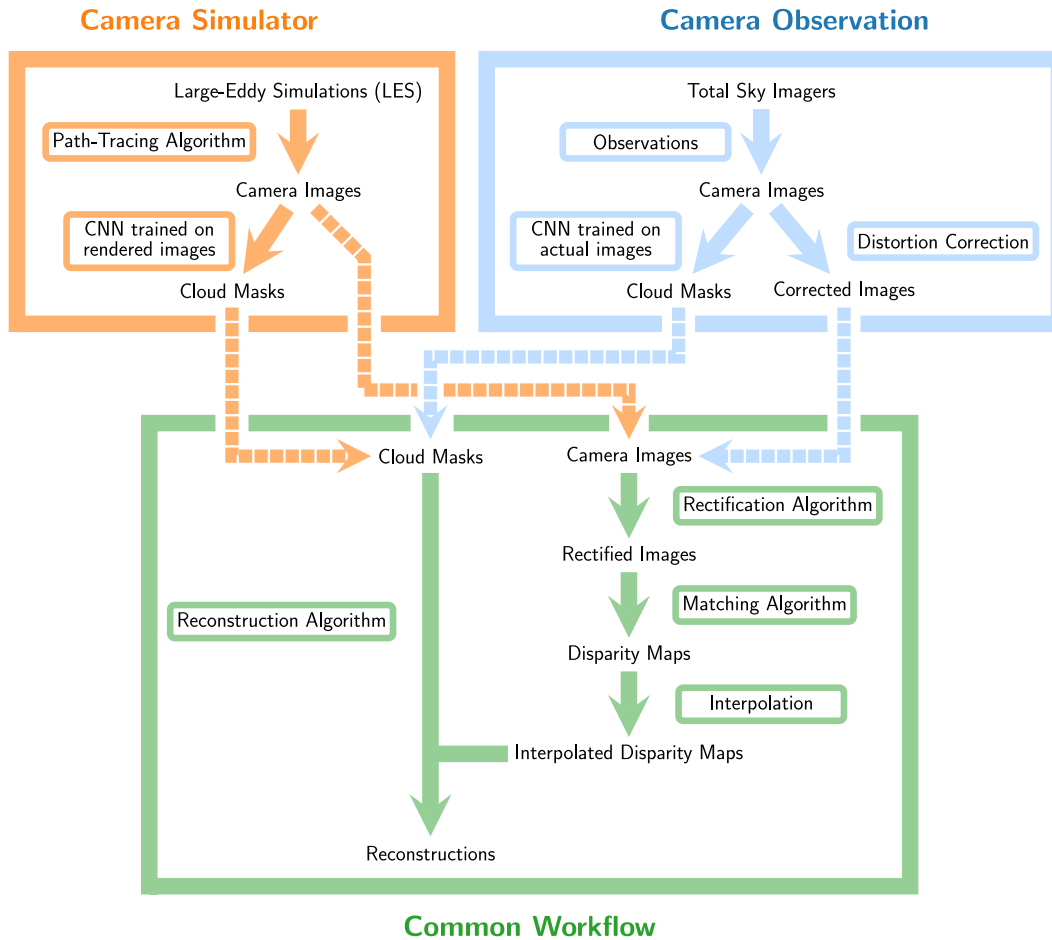

Figure 1. Schematic workflow for reconstructing cloud fields. Orange arrows represent methods specific to the camera simulator, while blue arrows denote methods specific to camera observations. Green arrows highlight the shared steps in the workflow.

For CNN training, six manually selected images per camera are used to capture the environmental variations around the camera. These images are labeled by visually identifying and marking white cloud pixels as clouds, serving as the ground truth for cloud masking, as no definitive cloud mask reference exists. To account for diurnal variations, the selected images cover three time points (09:30, 12:00, and 17:00 UTC) for both days and both cameras. In the controlled LES setup, which maintains a stable environment, only six images of one camera are selected (specifically at 09:00, 12:05, and 17:00 UTC for both days). All training images and their corresponding cloud masks are available in the supplementary data publication (Burchart et al., 2025). The CNN model is trained for 1,000 epochs, with the training loss beginning to increase after approximately 550 epochs. As a result, the model trained for 500 epochs is selected for the analysis in this study.

To validate the CNN cloud mask algorithm, we visually compared each cloud mask with the RGB color-based threshold method described in Löhnert et al. (2015) for cloud cover calculation, and Beekmans et al. (2016) for 3D cloud field reconstruction. Figure 2 compares these methods applied to the same image. Both methods face challenges in differentiating the bright sun from clouds. However, the CNN method performs better, particularly by reducing false classifications of the sunlit circular camera surroundings as clouds. Additionally, objects like towers and measurement instruments, which the color-based method often misclassifies as clouds, are less frequently misidentified by the CNN. The CNN method also more accurately identifies dark cloud bases, a task where the threshold method used in Beekmans et al. (2016) struggles. These observations are consistent across all tested images, even though only one example is shown here. Overall, the CNN cloud mask demonstrates significant improvements over the previous method.

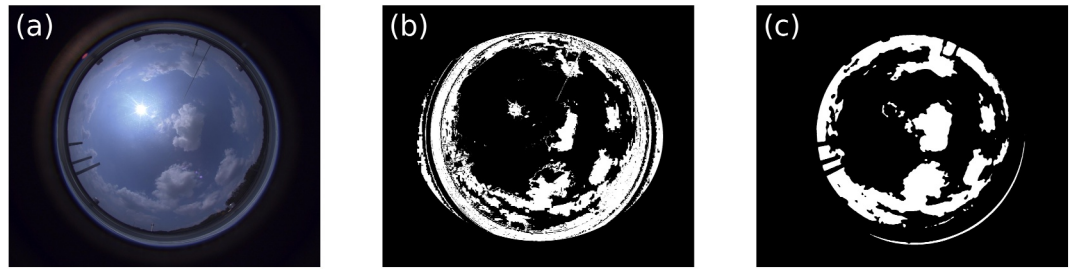

Figure 2. Cloud mask comparison: (a) Original camera image, (b) color-based cloud mask, and (c) CNN cloud mask implemented in this study.

2.3. Observational Data

Table 1 provides an overview of the observational data used in this study, along with the associated JOYCE instrumentation. For a more detailed description of the data, see Appendix A.

2.4. LES Model Setup

This study makes use of the Dutch Atmospheric Large-Eddy Simulation code (DALES, Heus et al., 2010). The DALES code has participated in numerous LES Model Intercomparison Studies (MIP) in the past that were dedicated to testing model performance for various modes of cumulus convection (e.g., Brown et al., 2002; de Roode et al., 2016; Schemann et al., 2020; Siebesma et al., 2003; Stevens et al., 2001; van der Dussen et al., 2013; van Zanten et al., 2011). For a brief overview of DALES, see Appendix B.

The design of the LES experiments used in this study in principle follows the standardized setup described in detail by Laar et al. (2019), which was specifically designed to simulate diurnal cycles of shallow convection observed at land sites. For a concise summary of the standardized setup, see Appendix B.

A few crucial differences are introduced in this general setup to further optimize performance concerning both the onset and height distribution of surface-driven shallow convective clouds on the 2 days of interest. These changes include the following:

1. Model initialization takes place at 06:00 UTC just before sunrise, herein following the LASSO model configuration as applied at the Atmospheric Radiation Measurement (ARM) Southern Great Plains (SGP) site (Gustafson et al., 2020);

Table 1
Overview of the Observational Data and Related Information

Instrument	Principle	Measurement quantity	Specifications	Atmospheric variables
Cameras	Cameras viewing the sky with a 185° FOV via fisheye projection	RGB images (2,456 × 2,054 pixels)	$\Delta t = 5$ min	cloud cover, cloud base height, cloud size distribution
Ceilometer CHM15k	Light detecting and ranging (lidar)	Backscatter profiles at 1,064 nm	$\Delta t = 15$ s, $\Delta z = 15$ m	cloud cover, cloud base height
Ceilometer CT25K	Lidar	Backscatter profiles at 905 nm	$\Delta t = 15$ s, $\Delta z = 30$ m	cloud cover, cloud base height
Cloudnet	Synergistic product from cloud radar, ceilometer, and microwave radiometer		$\Delta t = 30$ s, $\Delta z = 30$ m	cloud vertical extent, cloud phase
Doppler lidar Streamline	Doppler lidar	Backscatter and Doppler velocity profiles at 1,500 nm	$\Delta t \approx 2$ s, $\Delta z = 30$ m	mixing-layer height
Radiation measurements	Pyranometer	Global and diffuse radiation	$\Delta t = 1$ min	cloud cover
Radiosondes	Balloon-borne profile observations	various temperatures, humidity, pressure	$\Delta t \approx 1$ h	height, temperature, specific humidity

Table 2
Overview of the Configuration of the LES Experiments

Model	DALES
Number of grid cells × levels	512 × 512 × 144
Horizontal resolution	50 × 50 m^2
Horizontal domain	25.6 × 25.6 km^2
Model top	13 km
Vertical grid	Telescopic, 20 m at lowest level
Horizontal boundary conditions	Doubly-periodic
3D output frequency	5 min

2. Prescribed, time dependent surface sensible and latent heat flux are used as measured at a nearby flux station at Selhausen (Schmidt et al., 2022);
3. ERA5 profiles during day time are replaced by data from local radiosondes, launched hourly at the JOYCE site from 06:00 UTC onwards on the 2 days of interest;
4. Nudging is only applied above the convective boundary layer, at a relatively tight timescale of 3 hr.

These four steps together act to more effectively tie the mean model state to local measurements throughout the diurnal cycle.

An overview of key characteristics of the LES experiments is provided in Table 2, covering grid spacing, domain size, vertical grid, boundary conditions, and output specifics. Based on previous MIP results the adopted spatial resolution is considered high enough to resolve most of the variability and clouds associated with shallow convection. Because mesoscale organization is not the core focus of this study, a moderate horizontal domain size of 25.6 × 25.6 km^2 is thought sufficient for accommodating cloud populations large enough to yield statistically robust cloud size distributions (Neggers et al., 2003).

2.5. Rendering

A key component of the research work flow in this study is the use of rendered hemispheric images from LES cloud fields. To generate the rendered images the methodology of Burchart et al. (2024) is adopted. For a short summary on this approach see Appendix C. These rendered camera images are subsequently used to reconstruct the 3D cloud fields, employing the same method described in Section 2.2.

To further enhance the realism of the renderings, several modifications are made to the method of Burchart et al. (2024). Instead of fixed solar angles and power, solar positions and power are dynamically calculated based on the time and geographic location, with the solar angular diameter set to 0.53°. Additionally, anisotropic scattering with an asymmetry factor of 0.85 are used. The rendering process is sensitive to the minimum liquid water content threshold required to classify a grid box as a cloud. For the main results, this threshold is set to 0.002 g/kg, which approximates the minimum value observed in the 2-day simulations. The sensitivity of this threshold is further discussed in Appendix D.

2.6. Cloud Property Retrievals

2.6.1. Cloud Cover Retrieval

In this study five different cloud cover retrievals are used, as described below. Two retrievals from the camera images and one from the solar radiation, CloudNet, and the direct LES output.

To compute the cloud cover out of the camera images two methods are employed. The first method uses the 3D reconstruction (Section 2.2). The cloud cover is then estimated by projecting the 3D reconstruction points onto the 2D surface. The points are then triangulated using Delaunay tessellation, as implemented in the Python library SciPy (Virtanen et al., 2020). The cloudy area are determined by calculating the areas of the resulting triangles and summing them. To avoid connecting two separate clouds with triangles and erroneously adding the empty space between them to the cloud cover, triangles are excluded if any side exceeded 100 m.

The second method estimates cloud cover more directly from the images by applying the cloud mask explained in Section 2.2, counting the pixels identified as clouds, and dividing this number by the total number of pixels that would theoretically represent a fully cloud-covered sky. The final cloud cover estimate is obtained by averaging the results from the two camera images.

Cloud cover is derived from solar radiation measurements by analyzing the ratio between diffuse and global radiation as done by Butt et al. (2010). They use the ratio between calculated and observed global radiation as a proxy for cloudiness: if observed/calculated <0.8 then the observation is considered to be cloudy; otherwise it is classifie as cloud-free. This threshold value is usually considered constant. However, the method provides only reliable results for a solar zenith angle of less than 70° (Weber & Baker, 1982), as with a long optical path through the atmosphere, especially with the presence of aerosols, the diffuse fraction increases even for clear-sky cases.

Furthermore, this method can also cause biases due to spatial inhomogeneities of clouds in the direction of the sun position.

Cloud cover from CloudNet is derived by first detecting clouds within 2-hour sliding windows whenever liquid water cloud droplets are detected within 5 km. Then, the proportion of cloudy instances divided by the number of total measurements within the same window is taken. The same sliding window approach is also taken for the cloudy instances detected by the ceilometers and the solar radiation measurements.

The cloud cover from the direct LES output is estimated by identifying clouds by taking grid boxes with a liquid water content greater than zero. These cloud fields are vertically projected onto the 2D surface and the cloud cover is calculated from the LES grid by dividing the projected cloudy area by the total domain area.

2.6.2. Cloud Base Height Retrieval

The cloud base height of the reconstructed 3D cloud field are approximated by sorting the reconstruction points by height and selecting the 2.5th percentile. To prevent the inclusion of reconstruction points near the ground, such as buildings, towers, and trees, points below 500 m are excluded. In cases where few or no clouds were present, this led to cloud base height estimates close to 500 m. To avoid such inaccuracies, cloud base heights below 550 m are disregarded. Additionally, to ensure that only boundary layer cloud bases are considered, instances where the estimated cloud base height exceeded 4 km are removed.

Cloud base heights from the direct LES outputs are determined by identifying the lowest nonzero value in the domain-averaged cloud liquid water profile. To reduce noise in the cloud base height time series data, a median sliding window filter with a 15-min span was applied to the camera data, and 15-min minimum values were used for the ceilometer and Cloudnet measurements.

2.6.3. Estimating the Horizontal Cloud Size Distributions

To compute the hCSD the cloud fields are clustered into individual clouds using the DBSCAN algorithm (Density-Based Spatial Clustering of Applications with Noise) from the scikit-learn Python library (Ester et al., 1996; Pedregosa et al., 2011; Schubert et al., 2017).

For each cloud object i, the projected area A_i^P is calculated by vertically projecting the 3D points onto the 2D plane, and then using triangulation to determine the area, in the same way as for the cloud cover analysis (Section 2.2). The same procedure is applied to the cloud reconstructions based on emulated and actual camera images. For the 3D LES fields, the areas are calculated by summing up the area of the grid boxes on the projected plane that belong to each cloud object or cluster. The domain is thereby cropped to match the camera domain to ensure comparable results.

Figure 3 illustrates this method, showing the cloud fields after projection and triangulation. The black crosses represent camera locations, while the dotted box marks the region where reliable reconstructions can be achieved. When interpreting this figure, it should be noted that the camera method can primarily reconstruct cloud bases and portions of cloud sides that are visible to both cameras. Additionally, if any part of a cloud is obscured by other clouds in the camera's FOV, those obscured portions cannot be reconstructed (Burchart et al., 2024).

Following Neggers et al. (2019); Laar et al. (2019); Dawe and Austin (2012), A_i^P was transformed into a linear scale via:

$$l_i := \sqrt{A_i^P} \tag{1}$$

To sample the probability density function, the resulting cloud sizes, l_i, are then sorted into a histogram of cloud numbers $N(l)$, thereby approximating the underlining hCSD $\mathcal{N}(l)$ via:

$$\mathcal{N}(l) \approx \frac{N(l)}{dl}, \tag{2}$$

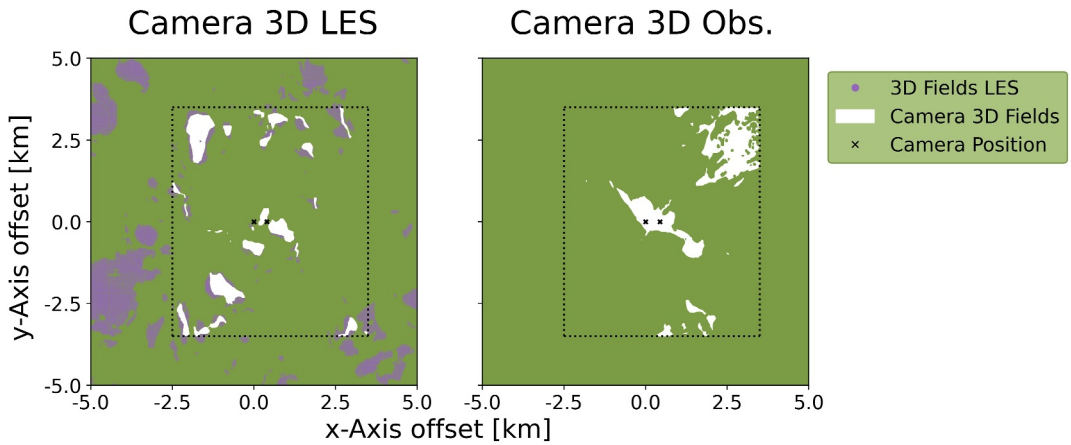

Figure 3. Vertically projected cloud fields from camera data (white) and LES output (purple dots). The dotted box indicates the cameras' effective Field-Of-View (FOV), where reliable reconstructions are feasible. Camera locations are marked with black crosses.

where *dl* represents the width of the size bins. For that, clouds are sorted into 20 logarithmically spaced bins from 100 m to maximum possible cloud size, following DeWitt et al. (2024); Wood and Field (2011); Neggers and Griewank (2022). Thereby, the same bins are used for all distributions.

The difference in slope of hCSDs can well be captured by fitting a functional form to the data. For observed hCSDs the power-law form has often been used to this purpose (Benner & Curry, 1998; Machado & Rossow, 1993; Neggers et al., 2003; Savre & Craig, 2023),

$$\mathcal{N}(l) \propto l^{-\alpha} \tag{3}$$

where l represents the cloud size, defined as the square root of the projected cloud area, and the power law slope α is a constant, typically ranging between approximately 1.7 and 2.5 (Rieck et al., 2014). The power-law approximation has been reported to hold across the entire detected size range (DeWitt et al., 2024; Yuan, 2011), while other studies have identified a scale break at cloud size l_{break} (Neggers & Griewank, 2022; Wood & Field, 2011; Xue & Feingold, 2006), with a different exponent α for clouds smaller and larger than l_{break}. Mathematically, that can be understood as a bounded or unbounded Pareto distribution. The unbounded Pareto distribution is given by the following cumulative distribution function F_{uP} and probability density function p_{uP} for an $\alpha > 1$ (White et al., 2008):

$$F_{\text{uP}}(\alpha; l) := \begin{cases} 1 - l_{\text{min}}^{\alpha-1} \cdot l^{1-\alpha} & \text{for } l \geq l_{\text{min}} \\ 0 & \text{for } l < l_{\text{min}} \end{cases}, \tag{4}$$

$$p_{\text{uP}}(\alpha; l) := \begin{cases} (\alpha - 1) \cdot l_{\text{min}}^{\alpha-1} \cdot l^{-\alpha} & \text{for } l \geq l_{\text{min}} \\ 0 & \text{for } l < l_{\text{min}} \end{cases} \tag{5}$$

In reality, however the sampled cloud sizes are always bounded by above by the maximum cloud sizes that fit in the observed domain. Therefore, it make sense to consider bounded Pareto distribution, which are defined by the following cumulative distribution function F_{bP} and probability density function p_{bP} (White et al., 2008):

$$F_{\text{bP}}(\alpha; l) := \frac{l_{\text{min}}^{1-\alpha} - l^{1-\alpha}}{l_{\text{min}}^{1-\alpha} - l_{\text{break}}^{1-\alpha}}, \quad p_{\text{bP}}(\alpha; l) := \frac{(\alpha - 1)}{l_{\text{min}}^{1-\alpha} - l_{\text{break}}^{1-\alpha}} \cdot l^{-\alpha} \quad \text{for } l_{\text{min}} \leq l \leq l_{\text{break}} \tag{6}$$

In this case l_{break} is either the maximum observable cloud size if the power law hold across the entire detected size range or the scale break. l_{min} is the smallest observable cloud size, in our case at least the 50 m LES resolution, and in theory at least the Kolmogorov length scale.

To compare the hCSDs found in this study to each other and to those reported in preceding studies, a similar power law fit is applied. For precession, the resulting power law slopes α are computed via two methods. The first method is by performing linear regression in the log-log space for the logarithmically binned histograms as done in DeWitt et al. (2024), Neggers and Griewank (2022); Neggers et al. (2019), Dawe and Austin (2012). The second method is based on maximum likelihood estimation (MLE) for given l_{min} and l_{break} as done in Savre and Craig (2023). To do this for a given sample of cloud sizes $\mathbf{l} := (l_i)_{i=1}^{n}$ in the range l_{min} and l_{break} the log-likelihood function

$$\ell(\alpha;\mathbf{l}) := \sum_{i=1}^{n} \log\left(p_{\text{bP}}(\alpha;l_i)\right) = n\log\left(\frac{\alpha-1}{l_{\text{min}}^{1-\alpha}-l_{\text{break}}^{1-\alpha}}\right) - \alpha\sum_{i=1}^{n}\log(l_i) \tag{7}$$

is maximized in regards of α by numerically approximating the root of its first derivative and ensuring that the its second derivative is negative, thereby using MINPACK's hybrd and hybrj routines as implemented in the scipy.optimize.root of the SciPy Python library (Virtanen et al., 2020). The calculation of the first and second derivatives are shown in Appendix E.

To assess uncertainty in the power-law slope estimation, the root mean square deviation (RMSD) is determined through a standard bootstrapping procedure. Specifically, the empirical data is resampled with replacement 2,500 times, and the best-fitting slopes (α) are repeatedly estimated.

A potential scale break is identified using a method similar to that of Savre and Craig (2023). First, all possible scale ranges ($l_{\text{min}}, l_{\text{break}}$) are considered by discretizing the full available size range in increments of 50 m, corresponding to the LES resolution. For each of these scale ranges, the best-fitting power-law slope $\hat{\alpha}$ are estimated using MLE and the Kolmogorv-Smirnov (KS) statistic is computed, which is defined by

$$D := \sup_{l_{\text{min}} < l < l_{\text{break}}} |F_{\text{e}}(l) - F_{\text{bP}}(\hat{\alpha};l)|, \tag{8}$$

where F_{e} is the empirical cumulative distribution (Savre & Craig, 2023). To enable a consistent comparison between the two hCSDs derived from camera data and the classic CSD, the same scale ranges ($l_{\text{min}}, l_{\text{break}}$) are used for each distribution. To ensure this consistency, the optimal range is selected as the one that minimizes the sum of the KS statistics across the three hCSDs for each possible Pareto distribution.

3. Case Description

This study focuses on non-precipitating shallow cumulus (ShCu) cloud fields observed on two consecutive days at the JOYCE observatory. To capture the complete diurnal cycle while ensuring sufficient daylight for the use of camera images, the period of analysis is here defined from 08:00 to 18:00 UTC on both days, corresponding to UTC+2 local time. The LES are initiated 2 hrs earlier to allow for turbulence spin-up. A data gap for the camera observations exists on 22 July between 08:50 and 09:30 UTC due to camera calibration.

Before comparing LES clouds to stereo camera data, it makes sense to first evaluate the general performance of the LES experiments for these 2 days, against other relevant data. The first step is to compare model profiles of water vapor specific humidity (q_v) and potential temperature (θ) against radiosonde data, as shown in Figure 4. To optimize statistical significance while still allowing interpretation of diurnal evolution, the profile data are averaged across three time intervals:

- *Early Morning*: 06:00–08:00 UTC
- *Late Morning*: 09:00–11:00 UTC
- *(After)Noon*: 11:00–14:00 UTC

In general, the LES reproduces the observed vertical thermodynamic structure and its diurnal evolution, with a few notable deviations. Water vapor specific humidity q_v and potential temperature θ both exhibit a well-mixed

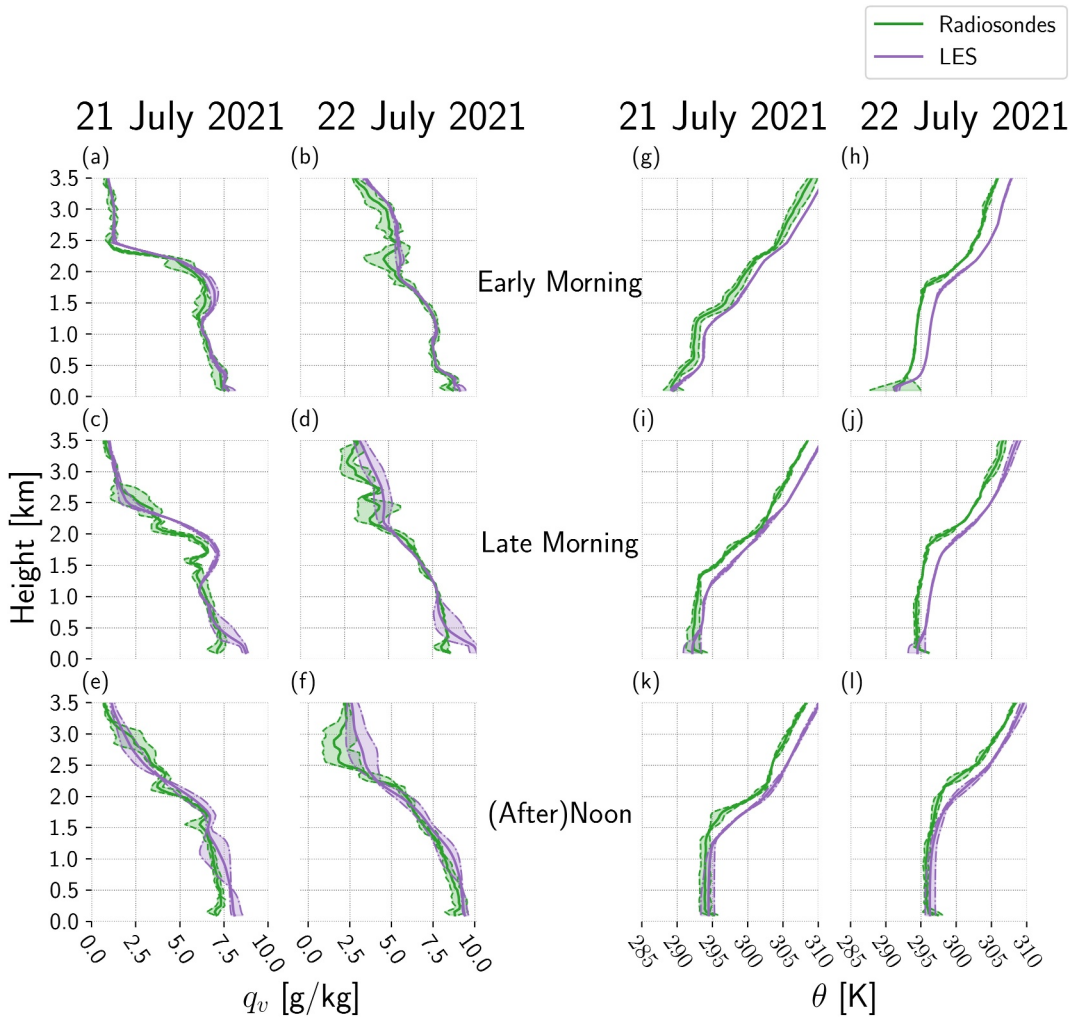

Figure 4. Diurnal Cycle of the averaged water vapor specific humidity profiles q_v (a–f) and potential temperature θ (g–l) of the selected contiguous ShCu days. Green indicates the radiosonde data, and blue the LES simulations. The shaded areas represent the min-max range within the averaging period.

layer situated beneath a conditionally unstable cloud layer, topped by an inversion layer. Minor discrepancies in q_v between model and measurements are present but are of second order compared to the ABL-deep structure, with average differences being less than 1 g kg^{-1}. A general warm bias exists of a few K, in particular at more elevated heights. We speculate this could be an artifact of the application of continuous Newtonian nudging above ABL top. By acting on the difference between the mean state and the (time-changing) nudging state, the nudging does allow such biases to exist, with their magnitude depending on the nudging time-scale.

Figure 5 compares the diurnal evolution of both mixed layer depth and cloud base height. Data on cloud top height was judged to be unreliable for these 2 days, and is excluded from the analysis (see Appendix F for a more elaborate explanation). Modeled mixed layer depth is based on the level of minimum buoyancy flux, following various previous studies (Burchart et al., 2024; Neggers, Stevens, & Neelin, 2007). For the Doppler lidar, the mixed-layer height is identified as the first level where the standard deviation of vertical velocity dropped below 0.4 m/s, adopting the method described by Schween et al. (2014). To ensure sampling consistency, 30-min averaged values are used in both methods. On both days the model underestimates the observed mixed layer deepening during the morning transition after sunrise. The lag of initial deepening could be due to underestimated turbulence generation in the model during the spin-up phase. However, at about 12:00 the model "catches up" with the observations, and mixed layer top is reproduced reasonably well during the afternoon, within a few 100 m.

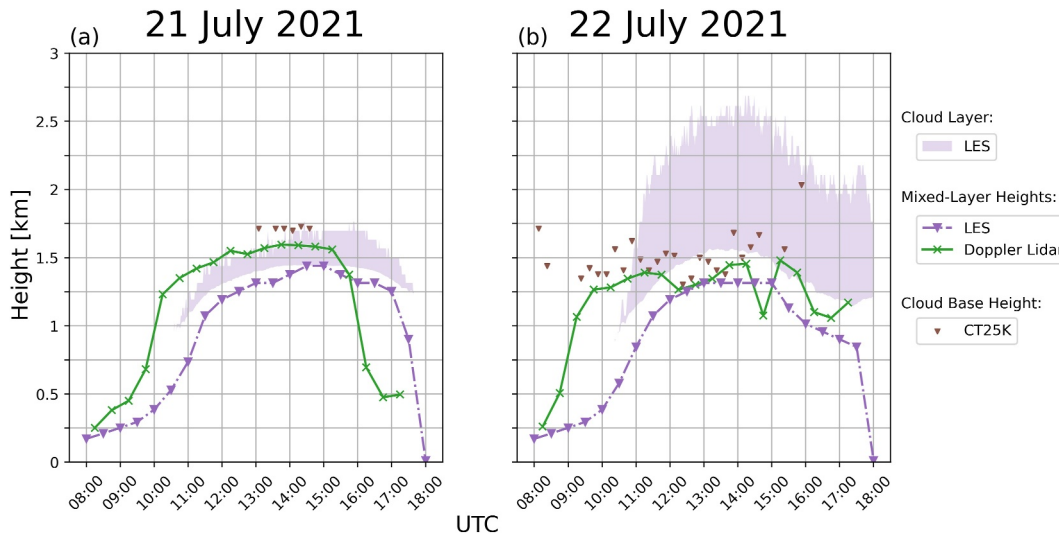

Figure 5. Diurnal cycle of (a) mixed-layer depth (lines) and (b) cloud occurrence (symbols and shading) for the two investigated days. Observed mixed layer depth is derived from Doppler lidar data (green), while cloud base height is derived from CT25K ceilometer data (small triangles). The methods applied to calculate these data, also for the LES model, are described in the text.

Associated with the underestimated initial deepening is a delay in cumulus cloud onset in the model on 22 July. This is evident when comparing ceilometer cloud base data to the LES cloud layer, as shown in Figure 5. Cloud base height is to some extent underestimated on 21 July, while better agreement is found on 22 July. Again, in the afternoon the model-observations agreement is better.

While the model-observation differences thus encountered are significant enough, it should be noted that such magnitudes are typical of LES based on limited data at meteorological sites (Endo et al., 2019; Gustafson et al., 2020; Neggers et al., 2012; Schemann et al., 2020; Zhang et al., 2017). These studies traced these biases to various possible sources, including uncertainties in the larger-scale forcings, initial and boundary conditions, spinup effects, and missing or underrepresented physics.

Do the encountered biases make the model simulations unfit for comparing model clouds to stereo camera analyses? All models are simplified representations of reality, and as a consequence, any model simulation is by definition not perfect. The main objective of this study is not to generate perfect reproductions of observed cloud fields, but rather to compare cloud field statistics in high resolution models, in all their shortcomings, to hemispheric images using a stereo camera simulator. Most observed cumulus clouds occur in the afternoon, when the vertical structure and cloud base height are generally reproduced. We use this agreement to justify comparing model clouds to stereo camera data in that period.

4. Results

With the evaluation of the mean vertical thermodynamic and cloud structure covered in the previous section, the next step is to focus on more advanced aspects of the cloud field as detectable by the stereo cameras. Thereby, the focus lies on the spatial structure of the cumulus cloud field, which is explored in this section.

4.1. Cloud Cover

The vertically projected cloud cover is investigated first, of which the retrieval methods for the various instruments were described in Section 2.6.1. The results are intercompared in Figure 6, also including model data. The top row presents the cloud cover retrievals from non-photogrammetric observations, while the bottom row represents camera-based retrievals, including those rendered from model fields. The camera-based data is calculated either through pixel-counting (labeled "Camera Pixel") or through reconstruction of the 3D cloud structures (labeled "Camera 3D"). The default and classic method of calculating cloud cover from 3D LES cloud

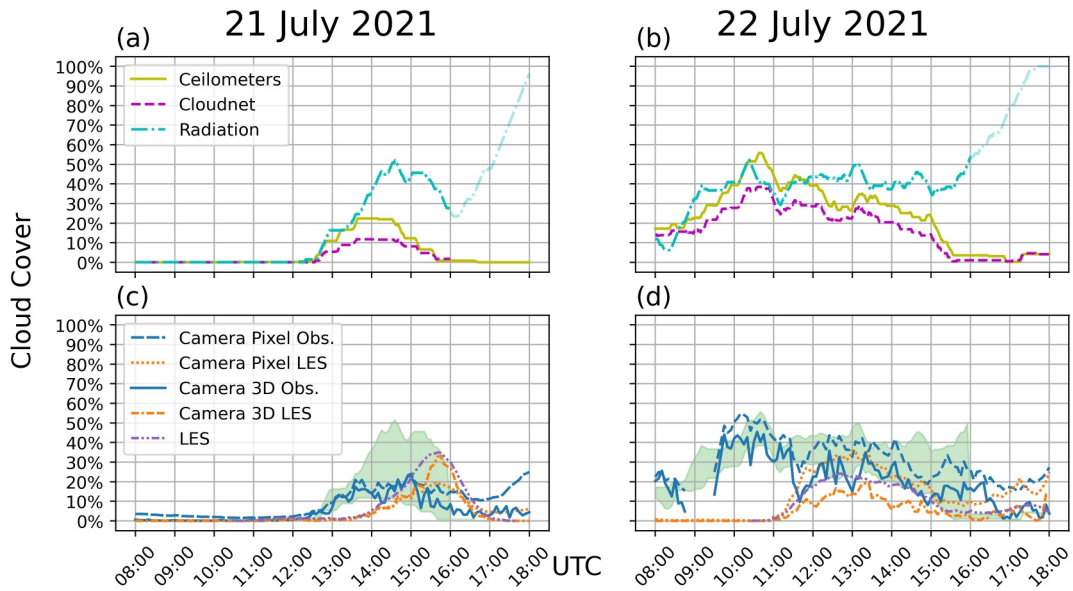

Figure 6. Time series of cloud cover from ground-based observations at JOYCE (top) compared to camera-based observations and LES results (bottom). "Camera Pixel Obs." and "Camera Pixel LES" refer to cloud cover from pixel counting of actual and rendered images, respectively. "Camera 3D Obs." and "Camera 3D LES" represent cloud field reconstructions from actual and rendered images. "LES" indicates cloud cover from LES. See Section 2.6.2 for retrieval details. The green shading in the bottom panel shows the min-max range from the top panel as a reference. No camera data were available between 08:50 and 09:30 UTC on 22 July 2021.

fields through vertical projection is also shown, for reference (labeled "LES"). To facilitate comparison of the top row to the bottom row, the minimum-maximum range of the top data is also shown in the lower panel.

Among the non-camera estimates, the radiation measurements start to deviate significantly from the other observations after 16:00 UTC. This is likely due to retrieval errors at large zenith solar angles, as longer optical paths increase diffuse radiation, particularly in the presence of aerosols. Reliable results are generally obtained when the zenith angle is less than 70° (Weber & Baker, 1982), which holds true before 17:00 UTC on both days. However, the substantial deviation already observed at 16:00 UTC suggests a high aerosol concentration, which is supported by sun photometer data [not shown], providing aerosol optical depth values exceeding 0.5 at 500 nm on both days. For this reason, the period after 16:00 UTC is shaded in the top row and excluded in the bottom row.

Moving on to the camera-based estimates, the cloud cover derived from the actual camera images (plotted in blue) generally aligns with the mean time evolution detected by the ground-based instrumentation. An interesting difference between pixel-based and 3D-based cloud cover emerges after 17:00 UTC on both dates, with the 3D-estimates remaining more or less stable while the pixel-estimates slightly increase. This likely results from the cloud-masking algorithm misclassifying the brightening sky near sunset as clouds.

On 22 July 2021 all observational datastreams agree remarkably well between 08:00–15:00 UTC, with deviations remaining below approximately 20%. One effect that is relevant when comparing vertically pointing instrumentation to hemispheric systems on both days is the fact that the latter also capture clouds in the periphery of the observation facility. As a result, fewer clouds are detected by the ceilometer and cloudnet datastreams. This effect explains some differences among the various data products shown in Figure 6, and is further elaborated on in Appendix G by means of example camera images.

The next step is to interpret the LES results on cloud cover in the light of these observational data. On both days the model reproduces the observed low cloud covers below four octas. The delayed cloud onset in LES as discussed earlier is clearly visible on both days. Encouragingly, after cloud onset the model reasonably approximates the diurnal cloud cover cycle, also in magnitude. In this later period the LES remains within 20% of the observed cloud cover range (green shaded area). Similar model deviations have been reported in previous studies making use of idealized LES of cumulus clouds over land (Brown et al., 2002; Gustafson et al., 2020; Zhang et al., 2017). In particular on 22 July the general decreasing trend in cloud cover is well reproduced by the model.

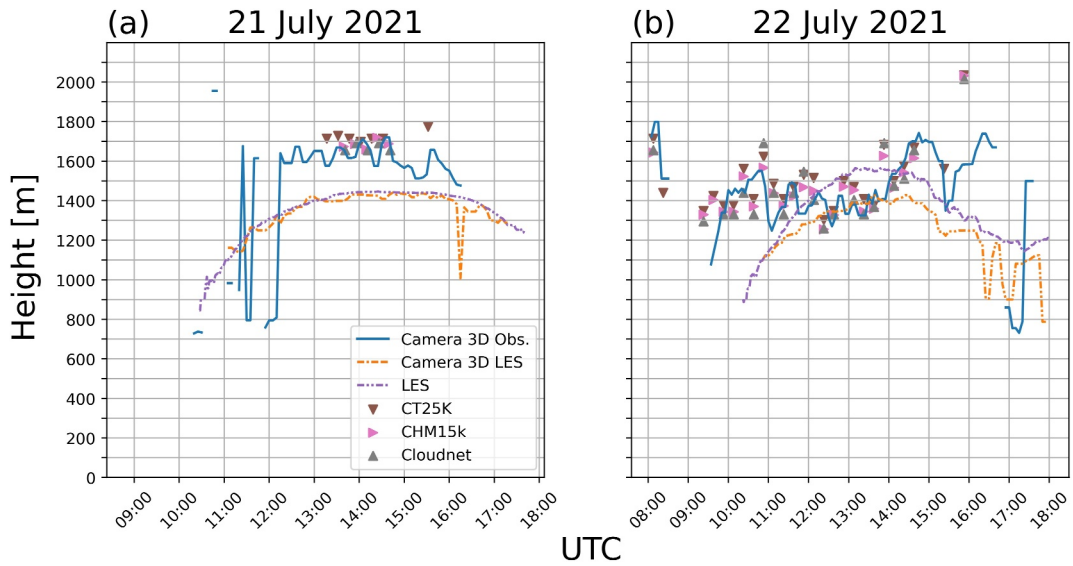

Figure 7. Comparison of cloud base heights from the camera data (rendered and actual images) with other observations at JOYCE and the direct LES output. No camera data were available from 08:50 to 09:30 UTC on 22 July 2021. Model results and camera observations are shown as continuous lines, expressing their high time availability.

The classic, vertically projected LES cloud cover is always close to the camera 3D method as applied to the model cloud fields. Another interesting feature is that the LES cover using pixel-counting persistently yields slightly higher cloud covers (on the order of 5%–10%) compared to the 3D method, an effect which is also consistently visible in the observations. This difference can likely be attributed to the fisheye projection used in camera images, which can include cloud sides which do not contribute to 3D reconstructions and vertical projections of cloud cover.

An important take-home message from these comparisons is that the idea of using hemispheric renderings of LES cloud fields seems feasible and reliable, and yields useful products that can well be used for evaluating such models against data from equivalent hemispheric observation systems. Overall, for calculating cloud cover we do not find clear advantages with the more complex 3D reconstruction method over the simpler pixel-counting approach. Both approaches perform comparably to the other instrumentation. This is particularly relevant for subsequent analyses, where these methods provide added value—especially for estimating cloud size distributions (see Section 4.3). These are difficult to obtain from 1D ground-based observations due to their limited spatial coverage.

4.2. Cloud Base Height

A second observable describing cumulus cloud spatial structure is the cloud base height (CBH), expressing the distribution of cloud presence in the vertical direction. While camera images do not capture the full vertical extent of clouds as for example, detected by cloud radar or microwave radiometers, the camera's wide FOV offers an advantage in estimating the cloud base height of heterogeneous cloud fields, particularly when there are few clouds directly above the measurement instruments.

Figure 7 inter-compares time series of cloud base height (see Section 2.6.2 for the retrieval methods), utlizing data from various sources: Camera-based cloud field reconstructions for the observational data (Camera 3D Obs.) and for the rendered images from the LES (Camera 3D LES), ceilometer measurements (CT25K and CHM15k), Cloudnet, and directly from the LES outputs (LES).

Under the first perspective—comparing camera observations (blue line) with other ground-based measurements (discrete points)—the CBH estimates from the camera-based method align well with the other instruments. Notable fluctuations in CBH detected by the cameras—before 12:30 UTC on 21 July and after 16:30 UTC on 22 July—coincide with periods of minimal cloud presence, as shown in Figure 6. On 21 July, non-hemispheric observations report CBH only between 13:00 and 15:30 UTC, whereas the camera-based method continuously

estimates CBH due to its wide FOV, capturing a greater number of clouds at any given time. This highlights a key advantage of the camera data over conventional pencil-beam observations.

Comparing the LES data with the camera observations of LES-rendered images—second perspective—the camera-based CBH estimates closely match the direct LES output on 21 July, with deviations of less than 50 m, except for a single peak between 16:00 and 17:00 UTC. On 22 July, the camera-based CBH underestimates the LES-derived values by up to 200 m, likely due to occasional cloud grid points being missed during the rendering process, as noted by Burchart et al. (2024).

Under the third perspective of comparing the observations against LES, the LES underestimates cloud base height by about 200 m on 21 July, while on 22 July the general cloud base height stays in the same range as the observations. However the LES shows a more pronounced diurnal cycle in cloud base height compared to the other observations for both days.

Overall, these comparisons strengthen the trust in the reconstruction and rendering method and highlight the added value of camera-based cloud field reconstructions in capturing spatially heterogeneous cloud scenes, offering continuous CBH estimates even when the other ground-based instruments have limited coverage.

4.3. Horizontal Cloud Size Distributions (hCSD)

A third way to express the spatial variability of cumulus cloud fields are horizontal Cloud Size Distributions (hCSD), which stands for the probability distribution of clouds as a function of their vertically projected size (see Section 2.6.3 for the estimation methods). As mentioned in the introduction, the hCSD has a rich history in the scientific investigation of cumulus cloud fields, going back decades. To link with these previous studies, the calculation and presentation of the hCSDs broadly follow the same approach.

Figures 8a and 8b shows the hCSDs across their full ranges for both days, the maximum cloud size of the hCSDs, l_{max}, and the power-law slopes with RMSD estimated using both methods are summarized in Table 3. Log-log axes are used so that any ranges with power law scaling appear as straight lines. The hCSDs with scale breaks are shown in Figures 8c and 8d and the power-law slopes estimated by both methods are summarized in Table 4, with RMSD.

In general, the hCSDs from all sources are similar in shape and range, and show an overall alignment. The fact that the hCSDs derived from the camera data, which could be referred to as *hemispheric hCSDs*, are similar to the "classic" hCSDs as derived from the 3D LES fields is encouraging. It demonstrates that camera data in principle provide a valuable, additional and independent source for analyzing hCSDs of cumulus cloud fields, and for evaluating these in LES models.

The power law fits in Figure 8, along with their associated slopes (α), are summarized in Table 3 and visualized in Figure 9a. This yields two new insights. Firstly, hemispheric hCSDs obtained from camera data, as characterized by their power law slope, are structurally similar between simulations and real cameras. Secondly, the non-hemispheric hCSDs directly computed from the 3D LES fields exhibit much steeper slopes, with a difference of about 0.5 with the hCSD derived using the hemispheric camera simulator. This difference is perhaps best visible in Figure 9a), and is evident on both days. It is also robust for the method used to estimate the power-law slope, as well as for the fitting range.

The non-hemispheric calculation of the hCSD results in more small clouds and fewer larger clouds. A Potential cause for their apparent difference could be the fact that cameras can only capture the unobscured portion of cloud hulls (Burchart et al., 2024).

These two findings are an important outcome of this study. They suggest that rendering hemispheric images from LES data, and then applying to them the same cloud reconstruction techniques as used for real observational camera images, offers an accurate method for confronting LES with camera data for evaluating cumulus cloud field heterogeneity. The results also indicate that care should be taken when comparing hemispheric to non-hemispheric cloud size distributions.

To further assess the consistency of these findings, the cloud size distributions are now stratified based on cloud cover, following Laar et al. (2019). They reported a dependence of the hCSD on cloud cover in the analysis domain, and identified a correlation between cloud cover and l_{max}, the largest cloud size in the population. The

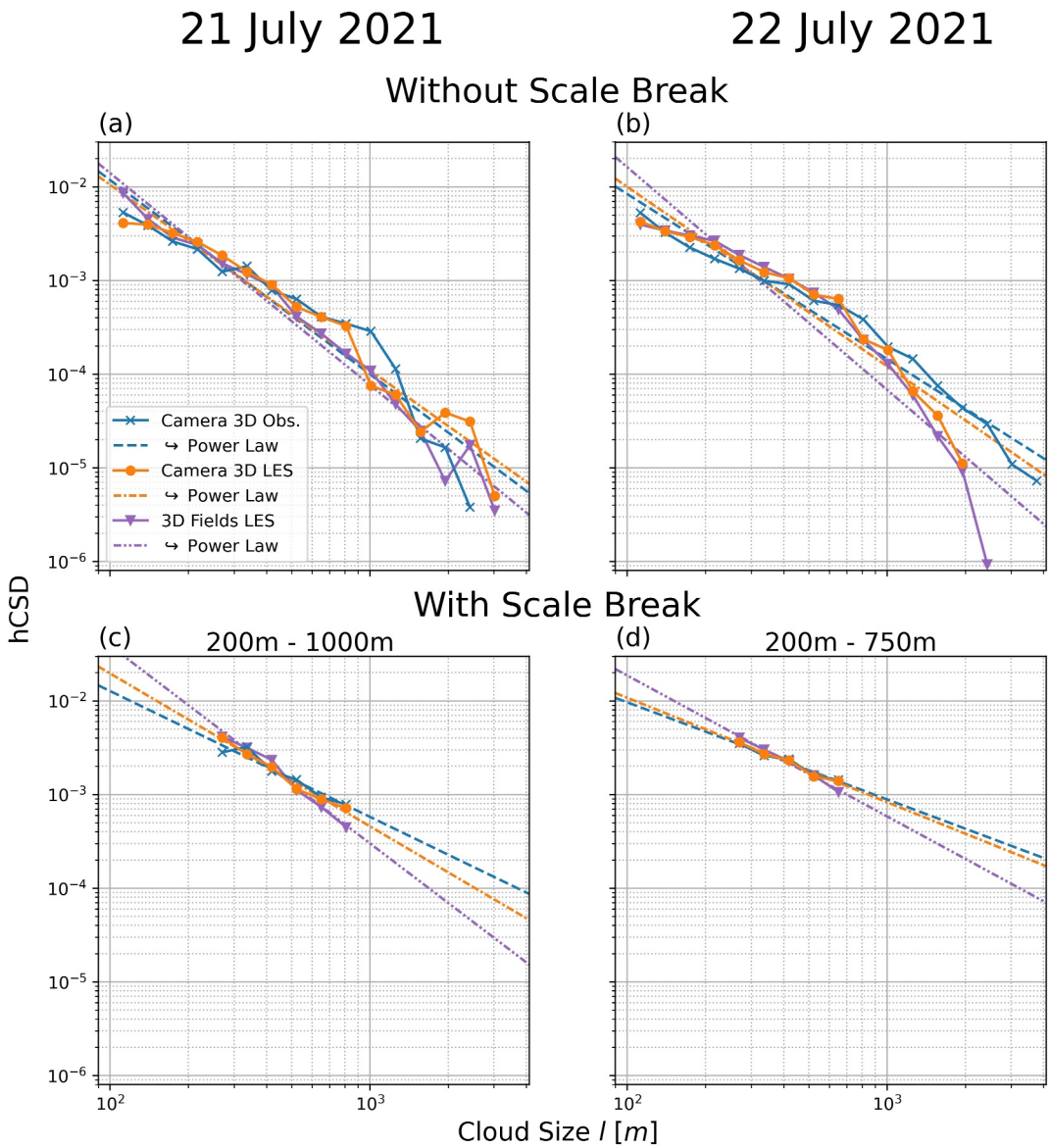

Figure 8. Comparison of hemispheric hCSDs of both emulated ("Camera 3D LES") and real images ("Camera 3D Obs."), as well as the non-hemispheric hCSDs calculated from the 3D LES field ("3D Fields LES"). The top row presents the full hCSD, while the bottom shows only the best fitting range of the hCSD, with binning adjusted accordingly. Straight thin lines represent linear fits in log-log space to the data shown.

cloud cover bins are defined as 0%–5%, 5%–10%, and 10%–15%, and the associated hCSDs are presented in Figure 10. Defining aspects of these hCSDs are summarized in Table 5, including l_{max}, the power-law slopes α from both methods together with their RMSD, and the number of clouds per bin. Figure 9b again visualizes the dependence of the slope on (a) the method of calculating the hCSD (horizontal axis) and (b) cloud cover in the analysis domain.

Stratifying on cloud cover implies a reduced number of clouds, with a outlying minimum of 30 clouds per bin as documented in Table 3. This still yielded hCSDs that appear reasonably well-defined. However, optimizing the scale ranges for these distributions proved impractical due to sample size limitations, with approximately 39% of cases containing fewer than 100 clouds. Consequently, these specific ranges and slopes are not shown.

Table 3
Maximum Cloud Size (l_{max}) and Power-Law Slope α With Root Mean Square Deviation (RMSD) From the Maximum Likelihood Estimation (MLE) and Linear Regression for the Cloud Size Distribution Without a Scale Break as Shown in Top Row of Figure 8

Days	Data	$l_{\max}[m]$	α from MLE	α from lin. reg.
21 July 2021	Camera 3D Obs.	2,546	1.79 ± 0.03	2.07 ± 0.11
	Camera 3D LES	2,784	1.81 ± 0.03	1.98 ± 0.09
	3D Fields LES	2,949	2.35 ± 0.04	2.26 ± 0.08
22 July 2021	Camera 3D Obs.	4,086	1.63 ± 0.02	1.76 ± 0.05
	Camera 3D LES	2,159	1.79 ± 0.02	1.92 ± 0.08
	3D Fields LES	2,645	1.92 ± 0.02	2.38 ± 0.21

All distributions still appear to express power-law scaling. Consistent with the findings of Laar et al. (2019), the slope of the hCSD reduces with cloud cover, while the maximum size $l_{\max}$ tends to increase. However, some deviations to this rule exist, which we speculate is due to poor sample size (i.e.., too few clouds). Similar to the previous analysis, the hCSDs calculated using camera methods are structurally similar between the observations and LES, and the slope of the non-hemispheric hCSD in LES tends to be larger. The overall conclusion is that the characteristics of the hCSD as established for the full data set are also still detectable for subsets based on cloud cover.

5. Discussion

A few considerations have to be made when interpreting the results obtained in this study. First, while the rendering algorithm used was initially assessed in Burchart et al. (2024), we improved it by incorporating adjustments for solar radiation and angle, which likely reduced error rates. However, as also documented in Appendix D for the cases studied here, the algorithm does contain sensitivity to the condensate mass threshold as used to define clouds in the model. This still needs further investigation.

Concerning cloud masking, this study advances previous methods (Beekmans et al., 2016; Burchart et al., 2024) by adopting a neural network approach instead of the threshold-based RGB method. Although an in-depth error analysis is hampered by the lack of ground truth data, the method remains flexible for future improvements in detection algorithms.

The hCSDs as shown in Figures 8 and 10 appear to follow power-law distributions, in line with prior studies (DeWitt et al., 2024; Neggers et al., 2019; Wood & Field, 2011). The existence of a scale break is affected by limitations in sample size due to the restricted domain sizes and the relatively small number of observed clouds, as discussed by previous studies (DeWitt et al., 2024; Neggers et al., 2019; Wood & Field, 2011). While acknowledging the impact of sample size, fully addressing this issue, or determining the exact shape of the underlying distribution function, is not the primary focus of this study. Further study is needed to gain insight.

The mean power law slopes of the hemispheric CSDs found in this study are inside, or close to, the range of values as previously published for "normal" non-hemispheric CSDs (Neggers et al., 2003; Rieck et al., 2014; Savre & Craig, 2023). These slopes are known to vary across seasons, surface type (marine vs. continental), cloud cover, spatial organization, and subsampling methods (Laar et al., 2019; Neggers et al., 2019; Senf et al., 2018). While comparison with such previously reported values can be instructive, perhaps most relevant is the structural difference in slope between hemispheric and non-hemispheric methods of calculating the CSD as found in this study. At least these are based on the same underlying data sets. Further research across multiple locations, bigger analysis domains and extended time frames is needed to allow more definite conclusions on the shape of the hCSD.

Table 4
Best Fitting Power-Law Ranges and Slopes α With Root Mean Square Deviations (RMSD) From Maximum Likelihood Estimation (MLE) and Linear Regression Fro the Cloud Size Distribution With Scale Break as Shown in the Bottom Row of Figure 8

Days	$l_{\min}[m]$	$l_{\text{break}}[m]$	Data	α from MLE	α from lin. reg.
21 July 2021	200	1,000	Camera 3D Obs.	1.31 ± 0.09	1.34 ± 0.13
			Camera 3D LES	1.78 ± 0.12	1.63 ± 0.26
			3D Fields LES	1.98 ± 0.09	2.11 ± 0.18
22 July 2021	200	750	Camera 3D Obs.	1.09 ± 0.09	1.04 ± 0.13
			Camera 3D LES	1.22 ± 0.11	1.12 ± 0.15
			3D Fields LES	1.52 ± 0.08	1.50 ± 0.11

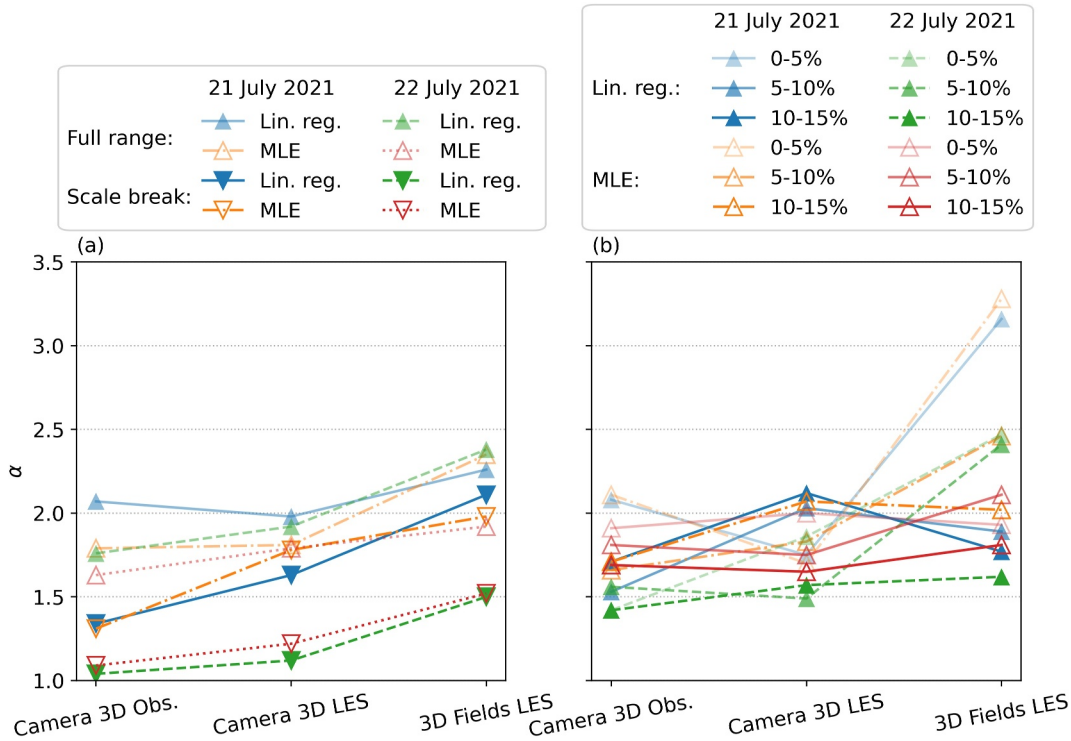

Figure 9. Visual summary of the powerlaw slopes as summarized in Tables 3 and 4 for panel (a), and Table 5 for panel (b). The position on the horizontal axis indicates the three methods of calculating the hCSD, as described in the text.

6. Concluding Remarks

This study combines the methodologies introduced by Burchart et al. (2024) and Beekmans et al. (2016) for (a) three-dimensionally reconstructing cloud fields from imagery by pairs of hemispheric cameras, and (b) the hemispheric ray-tracing rendering of LES cloud fields. The overall goal is to thus develop a "hemispheric stereo camera simulator" for efficiently and fairly evaluating the spatial structure of resolved cumuliform cloud fields in high resolution models against hemispheric camera data. Imagery from a network of hemispheric cameras at a meteorological site in western Germany is used to explore this method, supplemented with measurements by various ground-based remote sensing instrumentation providing classic pencil beam measurements of boundary layer clouds. Two consecutive diurnal cycles of shallow cumulus convection at the site were selected to test the simulator method. Dedicated LES experiments were conducted that were closely based on available measurements. A novelty is the calculation of hemispheric horizontal Cloud Size Distributions (hCSD) based on the 3D cloud field reconstructions, from both the real camera data and the rendered images of the LES clouds.

The main findings of this study can be briefly summarized as follows:

- For the two investigated days of summertime cumulus convection, cloud cover and cloud base height as derived from hemispheric camera data align well with independent measurements by vertically pointing ground-based instrumentation;
- Cloud field properties derived from rendered hemispheric images of LES clouds closely match with classic calculations directly based on full model fields, providing further confidence in this new technique based on ray-tracing;
- Pixel-based estimates of cloud cover from hemispheric imagery, either real or virtual, yield slightly larger values compared to 3D reconstructions;
- Good agreement is found between LES and camera observations in terms of the shape of the hemispheric hCSDs;

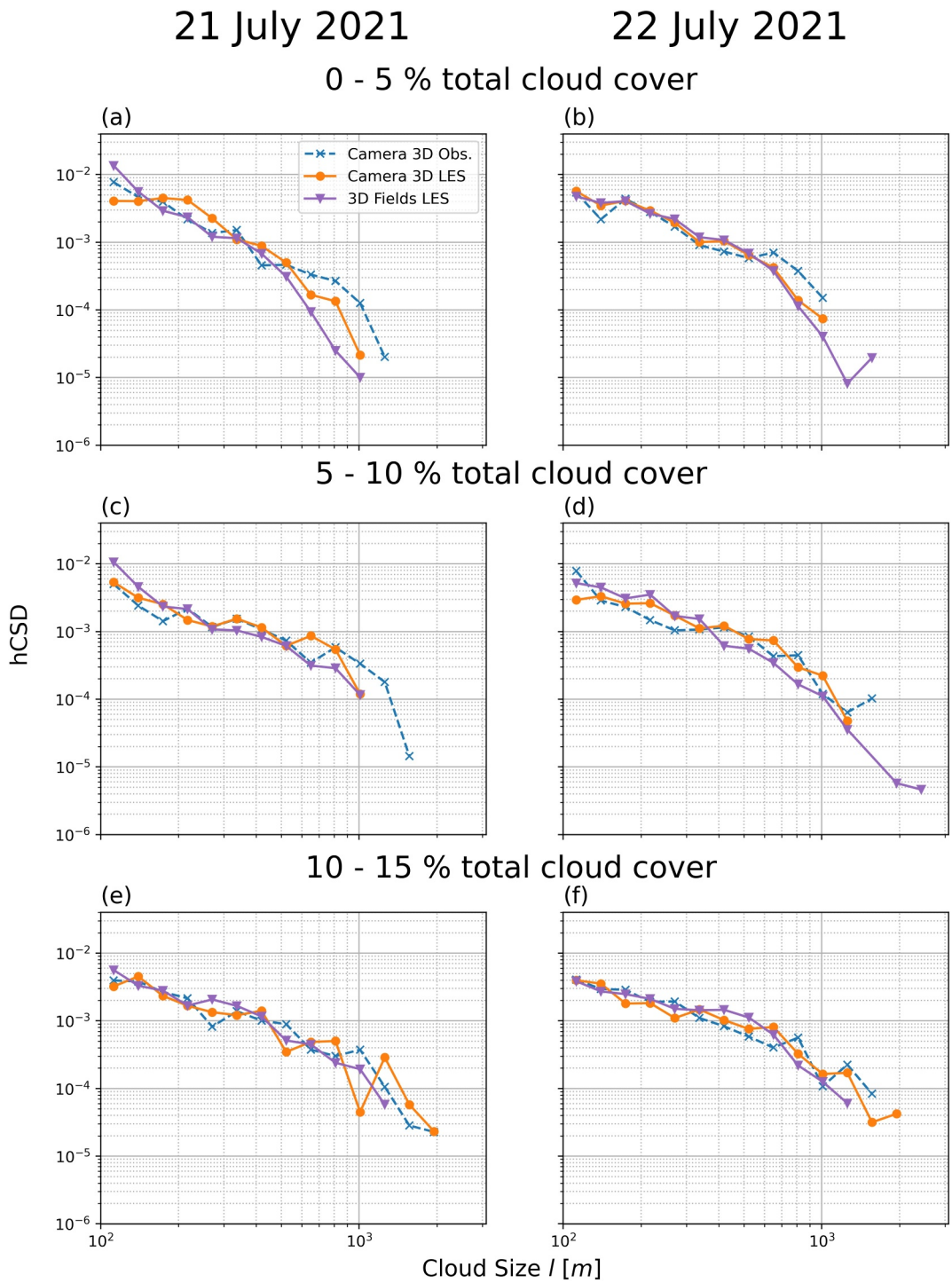

Figure 10. Comparison of hemispheric hCSDs of both emulated (Camera 3D LES) and real images (Camera 3D Obs.), as well as the non-hemispheric hCSDs of the 3D LES field for clouds grouped by total cloud cover.

- Hemispheric hCSDs exhibit substantially weaker power law slopes compared to distributions directly calculated from 3D fields through vertical projection;
- Stratifying the data set on cloud cover does not substantially alter these findings, despite the implied smaller sample sizes.

Table 5
Maximum Cloud Sizes ($l_{max}[m]$), the Best Fitting Slopes α From Both Methods, and the Number of Clouds for the hCSD Varying on Cloud Cover That Are Shown in Figure 10

	21 July 2021			22 July 2021		
	Obs.	Camera LES	LES	Obs.	Camera LES	LES
$l_{max}[m]$						
0%–5%	1,315	967	954	1,001	1,104	1,655
5%–10%	1,499	1,090	938	1,551	1,315	2,645
10%–15%	1,936	1,741	1,237	1,560	2,159	1,222
α from MLE						
0%–5%	2.11 ± 0.05	1.70 ± 0.05	3.28 ± 0.10	1.91 ± 0.15	2.05 ± 0.04	2.12 ± 0.04
5%–10%	1.66 ± 0.05	1.83 ± 0.06	2.46 ± 0.12	1.81 ± 0.08	1.75 ± 0.04	2.11 ± 0.05
10%–15%	1.71 ± 0.05	2.07 ± 0.08	2.02 ± 0.07	1.69 ± 0.05	1.65 ± 0.04	1.81 ± 0.05
α from lin. reg.						
0%–5%	2.08 ± 0.15	1.75 ± 0.09	3.16 ± 0.23	1.42 ± 0.28	1.86 ± 0.13	2.47 ± 0.17
5%–10%	1.53 ± 0.26	2.03 ± 0.23	1.89 ± 0.16	1.56 ± 0.15	1.49 ± 0.12	2.41 ± 0.20
10%–15%	1.71 ± 0.14	2.12 ± 0.22	1.77 ± 0.14	1.42 ± 0.11	1.57 ± 0.11	1.62 ± 0.15
number of clouds						
0%–5%	359	314	623	30	366	482
5%–10%	203	170	194	114	305	438
10%–15%	206	103	211	210	277	188

Overall, the results suggest that rendering LES output into synthetic camera images can be an additional and valuable method for gaining insight into the spatial structure of cloud fields, and for facilitating fair comparisons with real camera data. They particularly caution against directly comparing hemispheric cloud size distributions to non-hemispheric distributions. Care should be taken to use an hemispheric instrument simulator instead.

Appendix A: Supplementary Information on Observational Data

This study uses fisheye cloud image data captured by a dual-camera setup. The two cameras, positioned roughly 438.64 m apart, are both network cameras manufactured by *IDS Imaging Development Systems*—specifically, the uEye GigE UI–2280SE. Each camera is fitted with a $\frac{2}{3}''$ CCD sensor and uses a Fujinon FE185C057HA-1 C-Mount fisheye lens adapter, offering a field of view of 185° with a fixed focal length. The camera constant for both cameras is 550 pixels.

Ceilometers are simple lidar instruments that emit a laser beam in the near-infrared wavelength region and detect a signal which is backscattered by atmospheric constituents. Ceilometers are usually pointing vertically. Liquid clouds scatter the lidar beam very strongly, therefore the cloud base can be detected with a high accuracy. From the time difference between emitted and received signal, the distance of the scattering object can be determined. Ceilometers only observe a so-called "pencil beam", therefore individual non-uniformly distributed cloud field can cause a bias in the detected cloud cover.

Cloudnet (Illingworth et al., 2007) is a synergy product that combines vertically pointing ceilometer, cloud radar, and microwave radiometer. Cloudnet determines cloud phase and cloud vertical extent and provides a so-called target classification with a 30 s temporal and 30 m vertical resolution. The product has the same restrictions concerning non-uniform cloud fields as the ceilometer, however it can detect multiple cloud-base heights and also provides the cloud top height.

For validation of mixed-layer height, Doppler lidar observations is used. At JOYCE, a Streamline XR Doppler lidar by HALO photonics is operated continuously to observe boundary-layer properties as well as 3D wind profiles through different repetitive scan patterns. From vertical pointing observations, the variance of the vertical velocity can be derived which allows determining the mixing layer height by applying a variance threshold. Stable layers have a low vertical velocity variance whereas during well-mixed conditions this value is high. The method is described in Schween et al. (2014).

Appendix B: Supplementary Information on LES Model Setup

DALES uses prognostic equations under the Boussinesq approximation to a set of state variables, including wind components $\{u, v, w\}$, liquid water potential temperature Θ_l, total water specific humidity q_t, and various scalars. Cloud microphysics is represented using a double moment approach, predicting mass and number of a limited number of hydrometeor species. Resolved advection is calculated using a fifth-order central difference scheme, while transport on subgrid scales makes use of a prognostic turbulent kinetic energy (SFS-TKE) model (Deardorff, 1980). Time integration relies on a third-order Runge-Kutta scheme. A sponge layer is applied across the top quarter of model levels to remove spurious perturbations close to model top.

The standardized setup of Laar et al. (2019) can be summarized as follows: Initial conditions, lower boundary conditions and large-scale forcings are all sampled from ECMWF Reanalysis data (ERA5, Hersbach et al., 2020). Prescribed large-scale forcing is horizontally homogenous and time dependent, including horizontal advective tendencies for wind and thermodynamic state. Large-scale vertical advection is represented using a prescribed pressure velocity acting on the mean vertical profile. Radiation is interactive with the model state including clouds, making use of Monte Carlo Spectral Integration (Pincus & Stevens, 2009). The warm microphysics scheme of Seifert and Beheng (2006) is applied, featuring cloud liquid water and rain as prognostic hydrometeors. Continuous Newtonian nudging toward the ERA5 state is applied to prevent excessive drift in the model mean state, but weak enough to still allow resolved turbulence to act freely.

Appendix C: Supplementary Information on the Rendering Algorithm

The used rendering methodology (Burchart et al., 2024) utilizes the open-source 3D computer graphics software Blender (www.blender.org). In this approach, the liquid water content field from the LES defines cloudy grid boxes within Blender, with scattering and absorption properties determined by the spatial distribution of liquid water content. The images are rendered using path tracing, which approximates ground albedo and atmospheric conditions based on the sky model developed by Hosek and Wilkie (2012).

Appendix D: Liquid Water Sensitivity

As already mentioned in Section 2.5, the rendering algorithm is sensible to the minimum liquid water content need for a grid box to be considered as a cloud. Since volumes of few liquid water content seem to be situated near the cloud edge (Eytan et al., 2022), this affects also the retrieval of cloud base height from the cloud field reconstructions from the rendered images.

To analyze this effect the cloud base heights, as in Figure 7, are compared against the cloud base heights of reconstructions from rendered images where the minimum liquid water content threshold is changed to 1, 2, and 3 g/kg. The results are shown in Figure D1. As predicted the cloud base height increases consistently by increasing this threshold. However, determining which threshold is right is still an open question and seem to depend on the simulated scenario.

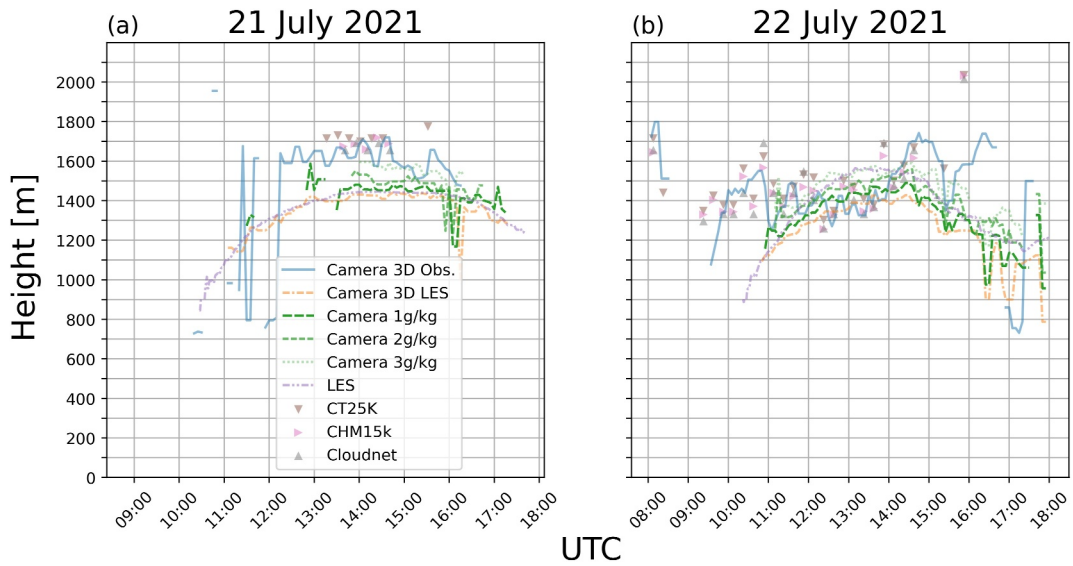

Figure D1. Same as Figure 7 but including the cloud base heights for rendered images using different liquid water content thresholds.

Appendix E: Log-Likelihood Derivatives

$$\frac{\partial \ell(\alpha;\mathbf{l})}{\partial \alpha} = \frac{\partial}{\partial \alpha}\left(n \log\left(\frac{\alpha-1}{l_{\min}^{1-\alpha} - l_{\text{break}}^{1-\alpha}}\right)\right) - \frac{\partial}{\partial \alpha}\left(\alpha \sum_{i=1}^{n} \log(l_i)\right) \tag{E1}$$

$$= n\left(\frac{l_{\min}^{1-\alpha} - l_{\text{break}}^{1-\alpha}}{\alpha-1}\right) \cdot \frac{\partial}{\partial \alpha}\left(\frac{\alpha-1}{l_{\min}^{1-\alpha} - l_{\text{break}}^{1-\alpha}}\right) - \sum_{i=1}^{n} \log(l_i) \tag{E2}$$

$$= n\left(\frac{l_{\min}^{1-\alpha} - l_{\text{break}}^{1-\alpha}}{\alpha-1}\right) \cdot \frac{l_{\min}^{1-\alpha} - l_{\text{break}}^{1-\alpha} - (\alpha-1)\cdot\frac{\partial}{\partial \alpha}\left(l_{\min}^{1-\alpha} - l_{\text{break}}^{1-\alpha}\right)}{\left(l_{\min}^{1-\alpha} - l_{\text{break}}^{1-\alpha}\right)^2} - \sum_{i=1}^{n} \log(l_i) \tag{E3}$$

$$= \frac{n}{\alpha-1} + \left(\frac{n}{\alpha-1}\right) \cdot \frac{-(\alpha-1)\left(-\log(l_{\min})\cdot l_{\min}^{1-\alpha} + \log(l_{\text{break}})\cdot l_{\text{break}}^{1-\alpha}\right)}{l_{\min}^{1-\alpha} - l_{\text{break}}^{1-\alpha}} - \sum_{i=1}^{n} \log(l_i) \tag{E4}$$

$$= \frac{n}{\alpha-1} + n \cdot \frac{\log(l_{\min})\cdot l_{\min}^{1-\alpha} - \log(l_{\text{break}})\cdot l_{\text{break}}^{1-\alpha}}{l_{\min}^{1-\alpha} - l_{\text{break}}^{1-\alpha}} - \sum_{i=1}^{n} \log(l_i) \tag{E5}$$

$$\frac{\partial^2 \ell(\alpha;\mathbf{l})}{\partial \alpha^2} = \frac{-n}{(\alpha-1)^2} + n \cdot \frac{\left(l_{\min}^{1-\alpha} - l_{\text{break}}^{1-\alpha}\right)\cdot\frac{\partial}{\partial \alpha}\left(\log(l_{\min})\cdot l_{\min}^{1-\alpha} - \log(l_{\text{break}})\cdot l_{\text{break}}^{1-\alpha}\right)}{\left(l_{\min}^{1-\alpha} - l_{\text{break}}^{1-\alpha}\right)^2} - n \cdot \frac{\left(\log(l_{\min})\cdot l_{\min}^{1-\alpha} - \log(l_{\text{break}})\cdot l_{\text{break}}^{1-\alpha}\right)\cdot\frac{\partial}{\partial \alpha}\left(l_{\min}^{1-\alpha} - l_{\text{break}}^{1-\alpha}\right)}{\left(l_{\min}^{1-\alpha} - l_{\text{break}}^{1-\alpha}\right)^2} \tag{E6}$$

$$= -\frac{n}{(\alpha-1)^2} + n \cdot \frac{\left(l_{\min}^{1-\alpha} - l_{\text{break}}^{1-\alpha}\right)\cdot\left(-\log(l_{\min})^2\cdot l_{\min}^{1-\alpha} + \log(l_{\text{break}})^2\cdot l_{\text{break}}^{1-\alpha}\right)}{\left(l_{\min}^{1-\alpha} - l_{\text{break}}^{1-\alpha}\right)^2} - n \cdot \frac{\left(\log(l_{\min})\cdot l_{\min}^{1-\alpha} - \log(l_{\text{break}})\cdot l_{\text{break}}^{1-\alpha}\right)\cdot\left(-\log(l_{\min})\, l_{\min}^{1-\alpha} + \log(l_{\text{break}})\, l_{\text{break}}^{1-\alpha}\right)}{\left(l_{\min}^{1-\alpha} - l_{\text{break}}^{1-\alpha}\right)^2} \tag{E7}$$

$$= -\frac{n}{(\alpha-1)^2} + n \cdot \frac{\left(-\log(l_{\min})^2 \cdot l_{\min}^{1-\alpha} + \log(l_{\text{break}})^2 \cdot l_{\text{break}}^{1-\alpha}\right)}{\left(l_{\min}^{1-\alpha} - l_{\text{break}}^{1-\alpha}\right)} + n \cdot \frac{\left(\log(l_{\min}) \cdot l_{\min}^{1-\alpha} - \log(l_{\text{break}}) \cdot l_{\text{break}}^{1-\alpha}\right)^2}{\left(l_{\min}^{1-\alpha} - l_{\text{break}}^{1-\alpha}\right)^2} \tag{E8}$$

$$= -\frac{n}{(\alpha-1)^2} + n \cdot \frac{\left(-\log(l_{\min})^2 \cdot l_{\min}^{1-\alpha} + \log(l_{\text{break}})^2 \cdot l_{\text{break}}^{1-\alpha}\right)}{\left(l_{\min}^{1-\alpha} - l_{\text{break}}^{1-\alpha}\right)} + n \cdot \frac{\log(l_{\min})^2 \cdot l_{\min}^{2-2\alpha} - 2\log(l_{\min}) \cdot l_{\min}^{1-\alpha} \log(l_{\text{break}}) \cdot l_{\text{break}}^{1-\alpha} + \log(l_{\text{break}})^2 \cdot l_{\text{break}}^{2-2\alpha}}{\left(l_{\min}^{1-\alpha} - l_{\text{break}}^{1-\alpha}\right)^2} \tag{E9}$$

$$= -\frac{n}{(\alpha-1)^2} + n \cdot \frac{\left(\log(l_{\min})^2 \cdot l_{\min}^{1-\alpha} \cdot l_{\text{break}}^{1-\alpha} + \log(l_{\text{break}})^2 \cdot l_{\text{break}}^{1-\alpha} \cdot l_{\min}^{1-\alpha}\right)}{\left(l_{\min}^{1-\alpha} - l_{\text{break}}^{1-\alpha}\right)^2} + n \cdot \frac{-2\log(l_{\min}) \cdot l_{\min}^{1-\alpha} \log(l_{\text{break}}) \cdot l_{\text{break}}^{1-\alpha}}{\left(l_{\min}^{1-\alpha} - l_{\text{break}}^{1-\alpha}\right)^2} \tag{E10}$$

$$= -\frac{n}{(\alpha-1)^2} + n \cdot l_{\min}^{1-\alpha} \cdot l_{\text{break}}^{1-\alpha} \cdot \frac{\log(l_{\min})^2 + \log(l_{\text{break}})^2 - 2\log(l_{\min})\log(l_{\text{break}})}{\left(l_{\min}^{1-\alpha} - l_{\text{break}}^{1-\alpha}\right)^2} \tag{E11}$$

$$= -\frac{n}{(\alpha-1)^2} + n \cdot l_{\min}^{1-\alpha} \cdot l_{\text{break}}^{1-\alpha} \cdot \frac{\left(\log(l_{\min}) - \log(l_{\text{break}})\right)^2}{\left(l_{\min}^{1-\alpha} - l_{\text{break}}^{1-\alpha}\right)^2} \tag{E12}$$

Appendix F: Cloudnet

Figure F1 is a repeat of Figure 5 but now showing CloudNet data for the 2 days of interest. The colors represent the various hydrometeor classes as yielded by its standard classification algorithm. The verticality of the CloudNet droplet class, visible in particular on 22 July, is an artifact of cloud top height of the low cumulus cloud layer not being captured properly by the radar data.

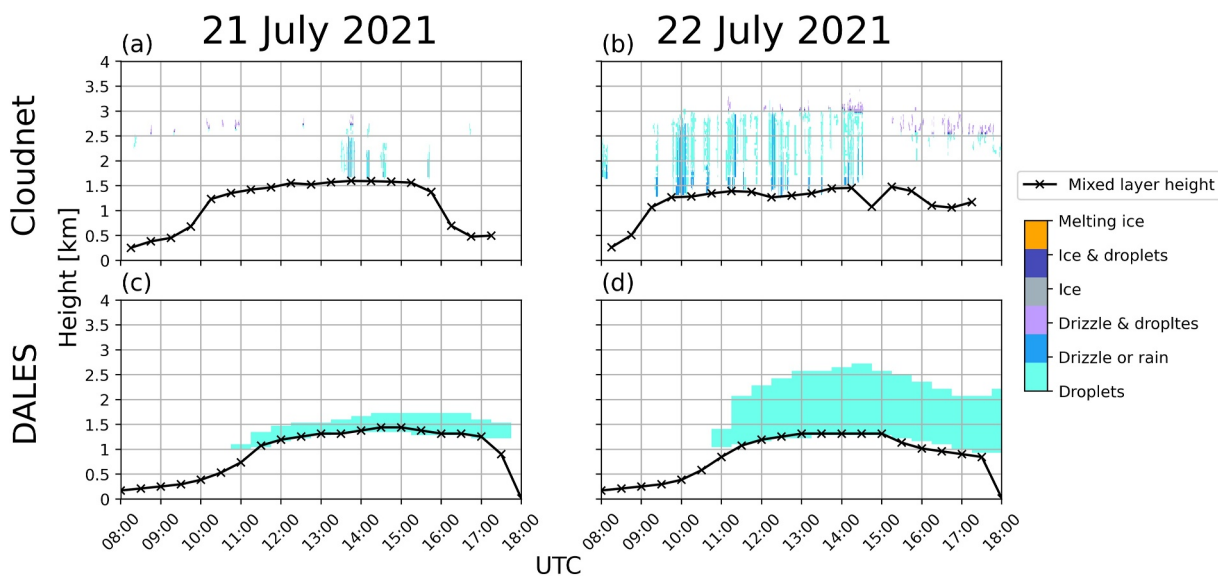

Figure F1. Same as Figure 5 but now showing CloudNet data. The lower panels show the LES cloud mask, for reference.

Appendix G: Visual Camera Image Analysis

Figure G1 presents the camera images from 22 July 2021, covering the period from 15:30 UTC to 18:00 UTC. The camera is positioned less than 10 m from both ceilometers. Consequently, if a cloud is detected by the ceilometers and is also visible in the camera images, it should appear near the center of the frame. However, the images reveal that clouds were primarily located toward the periphery, rather than directly overhead. This explains the near-zero cloud cover derived from the ceilometer measurements, as shown in Figure 6. This pattern is consistent throughout the period, including the intervals between the displayed images.

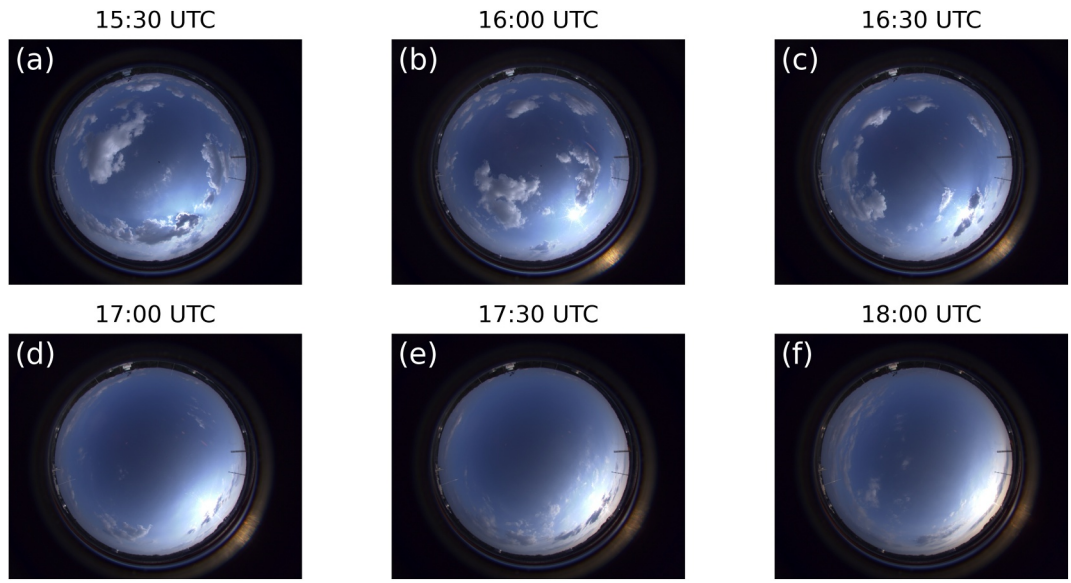

Figure G1. Camera images from 22 July 2021 for the camera located near the ceilometer observations.

Conflict of Interest

The authors declare no conflicts of interest relevant to this study.

Data Availability Statement

The data set to reproduce the results is available at https://doi.org/10.5281/zenodo.15498017 (Burchart et al., 2025). It contains the DALES configuration files and selected output files, the (rendered and actual) camera images and their cloud masks, their camera-based reconstructions, the cloud base heights, cloud base areas, and cloud cover of the reconstructions, the radiosondes, ceilometer, and Cloudnet measurements, the cloud cover from the radiation measurements, the mixed-layer height derived from the Doppler lidar, and scripts to reproduce the analysis and figures. The DALES version used (dales 4.3) is available at https://doi.org/10.5281/zenodo.5642477 (van Heerwaarden et al., 2021).

Acknowledgments
This research was supported by the U.S. Department of Energy's Atmospheric System Research, an Office of Science Biological and Environmental Research program, under grant DE-SC0022126 and by the German Research Foundation (DFG) under project number 430226822 (https://gepris.dfg.de/gepris/projekt/430226822). The Gauss Centre for Supercomputing e.V. (https://www.gauss-centre.eu/) is acknowledged for providing computing time on the Gauss Centre for Supercomputing (GCS) supercomputer JUWELS at the Jülich Supercomputing Centre (JSC) under the projects RCONGM and VIRTUALLAB. JOYCE data were provided by the Institute for Geophysics and Meteorology of the University of Cologne. JOYCE is a collaborative research platform between University of Cologne and Forschungszentrum Jülich within the European research infrastructure ACTRIS. We acknowledge ACTRIS and the Finnish Meteorological Institute for providing Cloudnet data which is available for download from https://cloudnet.fmi.fi. We acknowledge ECMWF for providing IFS model data. We thank two anonymous reviewers for their insightful comments and suggestions that significantly improved the manuscript. YB conceptualized the research idea with significant guidance from RN. BP and YB conducted the radiosonde measurements and collaboratively developed the method for determining mixing-layer heights from the observations. RN designed the model framework and strategy, prepared the model forcing files, and executed the LES simulations. BP calculated cloud cover using radiation measurements. YB improved and applied the Path-Tracer Algorithm to render cloud images from the LES data. YB developed the CNN cloud mask algorithm, which is also used to improve the Reconstruction Algorithm, and computed the reconstructions from both actual and rendered images. YB handled the data preprocessing, analysis, and visualization. BP contributed by writing the section on observational data, while RN authored Section 2.3 on the LES Model Setup. YB drafted the remainder of the manuscript, which underwent revisions by RN and BP. YB and RN jointly analyzed and interpreted the results, benefiting from BP's valuable insights regarding the observational data. YB curated the research data. Open Access funding enabled and organized by Projekt DEAL.

References

Angevine, W. M., Olson, J., Kenyon, J., Gustafson, W. I., Endo, S., Suselj, K., & Turner, D. D. (2018). Shallow cumulus in WRF parameterizations evaluated against LASSO large-eddy simulations. *Monthly Weather Review*, *146*(12), 4303–4322. https://doi.org/10.1175/MWR-D-18-0115.1

Beekmans, C., Schneider, J., Läbe, T., Lennefer, M., Stachniss, C., & Simmer, C. (2016). Cloud photogrammetry with dense stereo for fisheye cameras. *Atmospheric Chemistry and Physics*, *16*(22), 14231–14248. https://doi.org/10.5194/acp-16-14231-2016

Benner, T. C., & Curry, J. A. (1998). Characteristics of small tropical cumulus clouds and their impact on the environment. *Journal of Geophysical Research*, *103*(D22), 28753–28767. https://doi.org/10.1029/98JD02579

Blum, N. B., Nouri, B., Wilbert, S., Schmidt, T., Lünsdorf, O., Stührenberg, J., et al. (2021). Cloud height measurement by a network of all-sky imagers. *Atmospheric Measurement Techniques*, *14*(7), 5199–5224. https://doi.org/10.5194/amt-14-5199-2021

Brown, A. R., Cederwall, R. T., Chlond, A., Duynkerke, P. G., Golaz, J.-C., Khairoutdinov, M., et al. (2002). Large-eddy simulation of the diurnal cycle of shallow cumulus convection over land. *Quarterly Journal of the Royal Meteorological Society*, *128*(582), 1075–1093. https://doi.org/10.1256/003590002320373210

Burchart, Y., Beekmans, C., & Neggers, R. (2024). A stereo camera simulator for large-eddy simulations of continental shallow cumulus clouds based on three-dimensional path-tracing. *Journal of Advances in Modeling Earth Systems*, *16*(3), e2023MS003797. https://doi.org/10.1029/2023MS003797

Burchart, Y., Pospichal, B., & Neggers, R. (2025). Confronting large-eddy simulations with stereo camera data by means of reconstructed hemispheric cloud size distributions [Dataset]. https://doi.org/10.5281/zenodo.15498017

Butt, N., New, M., Malhi, Y., da Costa, A. C. L., Oliveira, P., & Silva-Espejo, J. E. (2010). Diffuse radiation and cloud fraction relationships in two contrasting Amazonian rainforest sites. *Agricultural and Forest Meteorology*, *150*(3), 361–368. https://doi.org/10.1016/j.agrformet.2009.12.004

Corbetta, G., Orlandi, E., Heus, T., Neggers, R., & Crewell, S. (2015). Overlap statistics of shallow boundary layer clouds: Comparing ground-based observations with large-eddy simulations. *Geophysical Research Letters*, *42*(19), 8185–8191. https://doi.org/10.1002/2015GL065140

Crispel, P., & Roberts, G. (2018). All-sky photogrammetry techniques to georeference a cloud field. *Atmospheric Measurement Techniques*, *11*(1), 593–609. https://doi.org/10.5194/amt-11-593-2018

Dawe, J. T., & Austin, P. H. (2013). Direct entrainment and detrainment rate distributions of individual shallow cumulus clouds in an LES. *Atmospheric Chemistry and Physics*, *13*(15), 7795–7811. https://doi.org/10.5194/acp-13-7795-2013

Dawe, J. T., & Austin, P. H. (2012). Statistical analysis of an LES shallow cumulus cloud ensemble using a cloud tracking algorithm. *Atmospheric Chemistry and Physics*, *12*(2), 1101–1119. https://doi.org/10.5194/acp-12-1101-2012

Deardorff, J. W. (1980). Stratocumulus-capped mixed layers derived from a three-dimensional model. *Boundary-Layer Meteorology*, *18*(4), 495–527. https://doi.org/10.1007/bf00119502

de Roode, S. R., Sandu, I., van der Dussen, J. J., Ackerman, A. S., Blossey, P., Jarecka, D., et al. (2016). Large-eddy simulations of Euclipse–gass Lagrangian stratocumulus-to-cumulus transitions: Mean state, turbulence, and decoupling. *Journal of the Atmospheric Sciences*, *73*(6), 2485–2508. https://doi.org/10.1175/JAS-D-15-0215.1

DeWitt, T. D., Garrett, T. J., Rees, K. N., Bois, C., Krueger, S. K., & Ferlay, N. (2024). Climatologically invariant scale invariance seen in distributions of cloud horizontal sizes. *Atmospheric Chemistry and Physics*, *24*(1), 109–122. https://doi.org/10.5194/acp-24-109-2024

Drönner, J., Korfhage, N., Egli, S., Mühling, M., Thies, B., Bendix, J., et al. (2018). Fast cloud segmentation using convolutional neural networks. *Remote Sensing*, *10*(11), 1782. https://doi.org/10.3390/rs10111782

Endo, S., Zhang, D., Vogelmann, A. M., Kollias, P., Lamer, K., Oue, M., et al. (2019). Reconciling differences between large-eddy simulations and Doppler Lidar observations of continental shallow cumulus cloud-base vertical velocity. *Geophysical Research Letters*, *46*(20), 11539–11547. https://doi.org/10.1029/2019GL084893

Ester, M., Kriegel, H.-P., Sander, J., & Xu, X. (1996). A density-based algorithm for discovering clusters in large spatial databases with noise. In *Proceedings of the Second International Conference on knowledge discovery and data mining* (pp. 226–231). AAAI Press.

Eytan, E., Khain, A., Pinsky, M., Altaratz, O., Shpund, J., & Koren, I. (2022). Shallow cumulus properties as captured by adiabatic fraction in high-resolution LES simulations. *Journal of the Atmospheric Sciences*, *79*(2), 409–428. https://doi.org/10.1175/JAS-D-21-0201.1

Fabel, Y., Nouri, B., Wilbert, S., Blum, N., Triebel, R., Hasenbalg, M., et al. (2022). Applying self-supervised learning for semantic cloud segmentation of all-sky images. *Atmospheric Measurement Techniques*, *15*(3), 797–809. https://doi.org/10.5194/amt-15-797-2022

Fielding, M. D., Schäfer, S. A. K., Hogan, R. J., & Forbes, R. M. (2020). Parametrizing cloud geometry and its application in a subgrid cloud-edge erosion scheme. *Quarterly Journal of the Royal Meteorological Society*, *146*(729), 1651–1667. https://doi.org/10.1002/qj.3758

Garrett, T. J., Glenn, I. B., & Krueger, S. K. (2018). Thermodynamic constraints on the size distributions of tropical clouds. *Journal of Geophysical Research: Atmospheres*, *123*(16), 8832–8849. https://doi.org/10.1029/2018JD028803

Griewank, P. J., Heus, T., Lareau, N. P., & Neggers, R. A. J. (2020). Size dependence in chord characteristics from simulated and observed continental shallow cumulus. *Atmospheric Chemistry and Physics*, *20*(17), 10211–10230. https://doi.org/10.5194/acp-20-10211-2020

Gustafson, W. I., Vogelmann, A. M., Li, Z., Cheng, X., Dumas, K. K., Endo, S., et al. (2020). The Large-Eddy Simulation (LES) Atmospheric Radiation Measurement (ARM) Symbiotic Simulation and Observation (LASSO) activity for continental shallow convection. *Bulletin of the American Meteorological Society*, *101*(4), E462–E479. https://doi.org/10.1175/BAMS-D-19-0065.1

Heinze, R., Dipankar, A., Henken, C. C., Moseley, C., Sourdeval, O., Trömel, S., et al. (2017). Large-eddy simulations over Germany using ICON: A comprehensive evaluation. *Quarterly Journal of the Royal Meteorological Society*, *143*(702), 69–100. https://doi.org/10.1002/qj.2947

Hersbach, H., Bell, B., Berrisford, P., Hirahara, S., Horányi, A., Muñoz-Sabater, J., et al. (2020). The ERA5 global reanalysis. *Quarterly Journal of the Royal Meteorological Society*, *146*(730), 1999–2049. https://doi.org/10.1002/qj.3803

Heus, T., & Seifert, A. (2013). Automated tracking of shallow cumulus clouds in large domain, long duration large eddy simulations. *Geoscientific Model Development*, *6*(4), 1261–1273. https://doi.org/10.5194/gmd-6-1261-2013

Heus, T., Van Heerwaarden, C. C., Jonker, H. J. J., Siebesma, P., Axelsen, S., Van den Dries, K., et al. (2010). Formulation of the Dutch Atmospheric Large-Eddy Simulation (DALES) and overview of its applications. *Geoscientific Model Development*, *3*(2), 415–444. https://doi.org/10.5194/gmd-3-415-2010

Hirschmuller, H. (2005). Accurate and efficient stereo processing by semi-global matching and mutual information. In *2005 IEEE computer Society Conference on Computer Vision and Pattern Recognition (CVPR'05)* (Vol. 2, pp. 807–814). https://doi.org/10.1109/CVPR.2005.56

Hosek, L., & Wilkie, A. (2012). An analytic model for full spectral sky-dome radiance. *ACM Transactions on Graphics*, *31*(95), 1–95:9. https://doi.org/10.1145/2185520.2185591

Illingworth, A. J., Hogan, R. J., O'Connor, E. J., Bouniol, D., Brooks, M. E., Delanoé, J., et al. (2007). CloudnetContinuous evaluation of cloud profiles in seven operational models using ground-based observations. *Bulletin of the American Meteorological Society*, *88*(6), 883–898. https://doi.org/10.1175/BAMS-88-6-883

Laar, T. W. v., Schemann, V., & Neggers, R. A. J. (2019). Investigating the diurnal evolution of the cloud size distribution of continental cumulus convection using multiday LES. *Journal of the Atmospheric Sciences*, *76*(3), 729–747. https://doi.org/10.1175/JAS-D-18-0084.1

Löhnert, U., Schween, J. H., Acquistapace, C., Ebell, K., Maahn, M., Barrera-Verdejo, M., et al. (2015). Joyce: Jülich observatory for cloud evolution. *Bulletin of the American Meteorological Society*, *96*(7), 1157–1174. https://doi.org/10.1175/BAMS-D-14-00105.1

Machado, L. A. T., & Rossow, W. B. (1993). Structural characteristics and radiative properties of tropical cloud clusters. *Monthly Weather Review*, *121*(12), 3234–3260. https://doi.org/10.1175/1520-0493(1993)121⟨3234:SCARPO⟩2.0.CO;2

Malkus, J., & Ronne, C. (1954). On the structure of some cumulonimbus clouds which penetrated the high tropical troposphere. *Tellus*, *6*(4), 351–366. https://doi.org/10.3402/tellusa.v6i4.8758

Myers, T. A., Scott, R. C., Zelinka, M. D., Klein, S. A., Norris, J. R., & Caldwell, P. M. (2021). Observational constraints on low cloud feedback reduce uncertainty of climate sensitivity. *Nature Climate Change*, *11*(6), 501–507. https://doi.org/10.1038/s41558-021-01039-0

Neggers, R., & Griewank, P. (2022). A decentralized approach for modeling organized convection based on thermal populations on microgrids. *Journal of Advances in Modeling Earth Systems*, *14*(10), e2022MS003042. https://doi.org/10.1029/2022MS003042

Neggers, R., Griewank, P., & Heus, T. (2019). Power-law scaling in the internal variability of cumulus cloud size distributions due to subsampling and spatial organization. *Journal of the Atmospheric Sciences*, *76*(6), 1489–1503. https://doi.org/10.1175/JAS-D-18-0194.1

Neggers, R., Heus, T., & Siebesma, A. (2011). Overlap statistics of cumuliform boundary-layer cloud fields in large-eddy simulations. *Journal of Geophysical Research*, *116*(D21). https://doi.org/10.1029/2011JD015650

Neggers, R., Jonker, H., & Siebesma, A. (2003). Size statistics of cumulus cloud populations in large-eddy simulations. *Journal of the Atmospheric Sciences*, *60*(8), 1060–1074. https://doi.org/10.1175/1520-0469(2003)60⟨1060:SSOCCP⟩2.0.CO;2

Neggers, R., Neelin, J., & Stevens, B. (2007a). Impact mechanisms of shallow cumulus convection on tropical climate dynamics. *Journal of Climate*, *20*(11), 2623–2642. https://doi.org/10.1175/JCLI4079.1

Neggers, R., Siebesma, A. P., & Heus, T. (2012). Continuous single-column model evaluation at a permanent meteorological supersite. *Bulletin of the American Meteorological Society*, *93*(9), 1389–1400. https://doi.org/10.1175/BAMS-D-11-00162.1

Neggers, R., Stevens, B., & Neelin, J. D. (2007b). Variance scaling in shallow-cumulus-topped mixed layers. *Quarterly Journal of the Royal Meteorological Society*, *133*(628), 1629–1641. https://doi.org/10.1002/qj.105

Nouri, B., Kuhn, P., Wilbert, S., Hanrieder, N., Prahl, C., Zarzalejo, L., et al. (2019). Cloud height and tracking accuracy of three all sky imager systems for individual clouds. *Solar Energy*, *177*, 213–228. https://doi.org/10.1016/j.solener.2018.10.079

Nuijens, L., & Siebesma, A. P. (2019). Boundary layer clouds and convection over subtropical oceans in our current and in a warmer climate. *Current Climate Change Reports*, *5*(2), 80–94. https://doi.org/10.1007/s40641-019-00126-x

Öktem, R., & Romps, D. M. (2021). Prediction for cloud spacing confirmed using stereo cameras. *Journal of the Atmospheric Sciences*, *78*(11). https://doi.org/10.1175/JAS-D-21-0026.1

Pedregosa, F., Varoquaux, G., Gramfort, A., Michel, V., Thirion, B., Grisel, O., et al. (2011). Scikit-learn: Machine learning in Python. *Journal of Machine Learning Research*, *12*, 2825–2830.

Pincus, R., & Stevens, B. (2009). Monte Carlo spectral integration: A consistent approximation for radiative transfer in large eddy simulations. *Journal of Advances in Modeling Earth Systems*, *1*(2). https://doi.org/10.3894/JAMES.2009.1.1

Plank, V. G. (1969). The size distribution of cumulus clouds in representative Florida populations. *Journal of Applied Meteorology and Climatology*, *8*(1), 46–67. https://doi.org/10.1175/1520-0450(1969)008⟨0046:TSDOCC⟩2.0.CO;2

Rieck, M., Hohenegger, C., & Heerwaarden, C. C. v. (2014). The influence of land surface Heterogeneities on cloud size development. *Monthly Weather Review*, *142*(10), 3830–3846. https://doi.org/10.1175/MWR-D-13-00354.1

Rodts, S. M. A., Duynkerke, P. G., & Jonker, H. J. J. (2003). Size distributions and dynamical properties of shallow cumulus clouds from aircraft observations and satellite data. *Journal of the Atmospheric Sciences*, *60*(16), 1895–1912. https://doi.org/10.1175/1520-0469(2003)060⟨1895:SDADPO⟩2.0.CO;2

Romps, D. M., & Öktem, R. (2018). Observing clouds in 4d with multiview stereophotogrammetry. *Bulletin of the American Meteorological Society*, *99*(12), 2575–2586. https://doi.org/10.1175/BAMS-D-18-0029.1

Savre, J., & Craig, G. (2023). Fitting cumulus cloud size distributions from idealized cloud resolving model simulations. *Journal of Advances in Modeling Earth Systems*, *15*(5), e2022MS003360. https://doi.org/10.1029/2022MS003360

Schemann, V., Ebell, K., Pospichal, B., Neggers, R., Moseley, C., & Stevens, B. (2020). Linking large-eddy simulations to local cloud observations. *Journal of Advances in Modeling Earth Systems*, *12*(12), e2020MS002209. https://doi.org/10.1029/2020MS002209

Schmidt, M., Becker, N., Dolfus, D., Esser, O., Graf, A., Kettler, M., & Mattes, J. (2022). Etc l2 archive, Selhausen Juelich, 2018-12-31–2022-09-30. Ecosystem Thematic Centre. Retrieved from https://hdl.handle.net/11676/GWgWkZJCp6nvA6m00ZE8wVYg

Schubert, E., Sander, J., Ester, M., Kriegel, H. P., & Xu, X. (2017). DBSCAN revisited, revisited: Why and how you should (still) use DBSCAN. *ACM Transactions on Database Systems*, *42*(3), 1–21. https://doi.org/10.1145/3068335

Schulz, H., Eastman, R., & Stevens, B. (2021). Characterization and evolution of organized shallow convection in the downstream North Atlantic trades. *Journal of Geophysical Research: Atmospheres*, *126*(17), e2021JD034575. https://doi.org/10.1029/2021JD034575

Schween, J. H., Hirsikko, A., Löhnert, U., & Crewell, S. (2014). Mixing-layer height retrieval with ceilometer and Doppler Lidar: From case studies to long-term assessment. *Atmospheric Measurement Techniques*, *7*(11), 3685–3704. https://doi.org/10.5194/amt-7-3685-2014

Seifert, A., & Beheng, K. D. (2006). A two-moment cloud microphysics parameterization for mixed-phase clouds. Part 1: Model description. *Meteorology and Atmospheric Physics*, *92*(1), 45–66. https://doi.org/10.1007/s00703-005-0112-4

Senf, F., Klocke, D., & Brueck, M. (2018). Size-resolved evaluation of simulated deep tropical convection. *Monthly Weather Review*, *146*(7), 2161–2182. https://doi.org/10.1175/MWR-D-17-0378.1

Shen, Z., Sridhar, A., Tan, Z., Jaruga, A., & Schneider, T. (2022). A library of large-eddy simulations forced by global climate models. *Journal of Advances in Modeling Earth Systems*, *14*(3), e2021MS002631. https://doi.org/10.1029/2021MS002631

Siebesma, A. P., Bretherton, C. S., Brown, A., Chlond, A., Cuxart, J., Duynkerke, P. G., et al. (2003). A large eddy simulation intercomparison study of shallow cumulus convection. *Journal of the Atmospheric Sciences*, *60*(10), 1201–1219. https://doi.org/10.1175/1520-0469(2003)60⟨1201:ALESIS⟩2.0.CO;2

Siebesma, A. P., & Jonker, H. J. J. (2000). Anomalous scaling of cumulus cloud boundaries. *Physical Review Letters*, *85*(1), 214–217. https://doi.org/10.1103/PhysRevLett.85.214

Stevens, B., Ackerman, A. S., Albrecht, B. A., Brown, A. R., Chlond, A., Cuxart, J., et al. (2001). Simulations of trade wind cumuli under a strong inversion. *Journal of the Atmospheric Sciences*, *58*(14), 1870–1891. https://doi.org/10.1175/1520-0469(2001)058⟨1870:SOTWCU⟩2.0.CO;2

Tiedtke, M. (1989). A comprehensive mass flux scheme for cumulus parameterization in large-scale models. *Monthly Weather Review*, *117*(8), 1779–1800. https://doi.org/10.1175/1520-0493(1989)117⟨1779:ACMFSF⟩2.0.CO;2

van der Dussen, J. J., de Roode, S. R., Ackerman, A. S., Blossey, P. N., Bretherton, C. S., Kurowski, M. J., et al. (2013). The gass/euclipse model intercomparison of the stratocumulus transition as observed during Astex: Les results. *Journal of Advances in Modeling Earth Systems*, *5*(3), 483–499. https://doi.org/10.1002/jame.20033

van Heerwaarden, C., Sjboeing, Ouwersloot, H., Thijsheus, Attema, J., Jansson, F., et al. (2021). jchylik/dales: Dales4.3_sb3 (version 4.3) [Software]. https://doi.org/10.5281/zenodo.5642477

van Zanten, M. C., Stevens, B., Nuijens, L., Siebesma, A. P., Ackerman, A. S., Burnet, F., et al. (2011). Controls on precipitation and cloudiness in simulations of trade-wind cumulus as observed during Rico. *Journal of Advances in Modeling Earth Systems*, *3*(2). https://doi.org/10.1029/2011MS000056

Virtanen, P., Gommers, R., Oliphant, T. E., Haberland, M., Reddy, T., Cournapeau, D., et al. (2020). SciPy 1.0: Fundamental algorithms for scientific computing in Python. *Nature Methods*, *17*(3), 261–272. https://doi.org/10.1038/s41592-019-0686-2

Weber, M. R., & Baker, C. B. (1982). Comments on" the ratio of diffuse to direct solar irradiance (perpendicular to the sun's rays) with clear skies–a conserved quantity throughout the day. *Journal of Applied Meteorology*, *21*(6), 883–886. https://doi.org/10.1175/1520-0450(1982)021<0883:corodt>2.0.co;2

White, E. P., Enquist, B. J., & Green, J. L. (2008). On estimating the exponent of power-law frequency distributions. *Ecology*, *89*(4), 905–912. https://doi.org/10.1890/07-1288.1

Wielicki, B. A., & Welch, R. M. (1986). Cumulus cloud properties derived using Landsat satellite data. *Journal of Applied Meteorology and Climatology*, *25*(3), 261–276. https://doi.org/10.1175/1520-0450(1986)025⟨0261:CCPDUL⟩2.0.CO;2

Wood, R., & Field, P. R. (2011). The distribution of cloud horizontal sizes. *Journal of Climate*, *24*(18), 4800–4816. https://doi.org/10.1175/2011JCLI4056.1

Xue, H., & Feingold, G. (2006). Large-eddy simulations of trade wind Cumuli: Investigation of aerosol indirect effects. *Journal of the Atmospheric Sciences*, *63*(6), 1605–1622. https://doi.org/10.1175/JAS3706.1

Yuan, T. (2011). Cloud macroscopic organization: Order emerging from randomness. *Atmospheric Chemistry and Physics*, *11*(15), 7483–7490. https://doi.org/10.5194/acp-11-7483-2011

Zhan, Y., Yi, F., Liu, F., Zhang, Y., Yu, C., & Zhou, J. (2021). Convective boundary layer clouds as observed with ground-based Lidar at a mid-latitude plain site. *Remote Sensing*, *13*(7), 1281. https://doi.org/10.3390/rs13071281

Zhang, Y., Klein, S. A., Fan, J., Chandra, A. S., Kollias, P., Xie, S., & Tang, S. (2017). Large-eddy simulation of shallow cumulus over land: A composite case based on ARM long-term observations at its Southern Great Plains site. *Journal of the Atmospheric Sciences*, *74*(10), 3229–3251. https://doi.org/10.1175/JAS-D-16-0317.1